

# On the Nonlinear Mapping of an Ocean Wave Spectrum Into a Synthetic Aperture Radar Image Spectrum and Its Inversion

KLAUS HASSELMANN AND SUSANNE HASSELMANN

*Max-Planck-Institut für Meteorologie, Hamburg, Germany*

A new, closed nonlinear integral transformation relation is derived describing the mapping of a two-dimensional ocean wave spectrum into a synthetic aperture radar (SAR) image spectrum. The general integral relation is expanded in a power series with respect to orders of nonlinearity and velocity bunching. The individual terms of the series can be readily computed using fast Fourier transforms. The convergence of the series is rapid. The series expansion is also useful in identifying the different contributions to the net imaging process, consisting of the real aperture radar (RAR) cross-section modulation, the nonlinear motion (velocity bunching) effects, and their various interaction products. The lowest term of the expansion with respect to nonlinearity order yields a simple quasi-linear approximate mapping relation consisting of the standard linear SAR modulation expression multiplied by an additional nonlinear Gaussian azimuthal cutoff factor. The cutoff scale is given by the rms azimuthal (velocity bunching) displacement. The same cutoff factor applies to all terms of the power series expansion. The nonlinear mapping relation is inverted using a standard first-guess wave spectrum as regularization term. This is needed to overcome the basic 180° mapping ambiguity and the loss of information beyond the azimuthal cutoff. The inversion is solved numerically using an iteration technique based on the successive application of the explicit solution for the quasi-linear mapping approximation, with interposed corrections invoking the full nonlinear mapping expression. A straightforward application of this technique, however, generally yields unrealistic discontinuities of the best fit wave spectrum in the transition region separating the low azimuthal wave number domain, in which useful SAR information is available and the wave spectrum is modified, from the high azimuthal wave number region beyond the azimuthal cutoff, where the first-guess wave spectrum is retained. This difficulty is overcome by applying a two-step inversion procedure. In the first step the energy level of the wave spectrum is adjusted, and the wave number plane rotated and rescaled, without altering the shape of the spectrum. Using the resulting globally fitted spectrum as the new first-guess input spectrum, the original inversion method is then applied without further constraints in a second step to obtain a final fine-scale optimized spectrum. The forward mapping relation and inversion algorithms are illustrated for three Seasat cases representing different wave conditions corresponding to weakly, moderately, and strongly nonlinear imaging conditions.

## 1. INTRODUCTION

Sea state can be completely characterized statistically by the two-dimensional directional wave spectrum  $F(\mathbf{k})$  describing the distribution of wave energy with respect to the wave propagation wave number  $\mathbf{k}$ . All statistical properties of an ocean wave field at any given location and time can be derived from this function. Unfortunately, however, the two-dimensional wave spectrum has proved notoriously difficult to measure. Verifications of wave models, which routinely compute the space-time distributions of  $F(\mathbf{k})$ , have therefore been based largely on one-dimensional frequency spectra derived from wave buoys or wave staffs. More recently, directional wave buoys, which provide at least some integrated information on the directional distribution, have been more frequently deployed, but even these data have been limited to relatively sparsely distributed locations. Measurements of the full two-dimensional spectrum have been obtained only at selected sites and for restricted time periods using large wave-staff arrays [e.g., *Donelan et al.*, 1985], or special remote sensing systems onboard aircraft [*Plant*, 1987], such as Radar Ocean-Wave Spectrometer (ROWS) [*Jackson*, 1981; *Jackson et al.*, 1985a, b], the surface contouring radar [*Kenney et al.*, 1979; *Walsh et al.*, 1985, 1987, 1991], or stereophotography [*Holthuijsen*, 1983].

The sparsity of directional wave data (together with the limited availability even of one-dimensional frequency spectra or integrated wave height data) has not only handicapped the verification of wave models, but has also deterred wave modelers from seriously addressing the problem of assimilating wave data into their models.

This situation could change dramatically in the 1990s. We look forward in this decade to extensive, in some cases continuous, global measurements of the two-dimensional wave spectrum from synthetic aperture radars (SARs) flown on satellites such as ERS 1 and 2, Radarsat, shuttle missions, and polar platforms. These data will be augmented by global significant wave height measurements from radar altimeters on ERS 1, 2, Topex-Poseidon, Spinsat, and other satellites. Furthermore, global sea surface wind data from satellite scatterometers and altimeters will provide improved wind fields as input for wave models. The simultaneous assimilation of these wind and wave data into global wave models and atmospheric forecast models offers exciting new opportunities and perspectives for wave modelers, but also presents major challenges to the wave- and weather-forecasting community.

This is exemplified by the SAR wave data. The potential of space-borne SARs for imaging two-dimensional ocean wave fields from space has been convincingly demonstrated by Seasat (cf. *Alpers* [1983], *Beal et al.* [1983], and other papers in the Seasat issue, *Journal of Geophysical Research*, volume 88, 1983) and the shuttle SIR-B mission [cf. *Alpers et al.*, 1986; *Brüning et al.*, 1988; *Monaldo and Lyzenga*, 1988].

Copyright 1991 by the American Geophysical Union.

Paper number 91JC00302.  
0148-0227/91/91JC-00302\$05.00

The theory of the SAR imaging of a moving ocean wave surface is now also rather well understood (cf. MARSEN SAR review [K. Hasselmann *et al.*, 1985], referred to in the following as MSR). The theory has been verified in a number of field experiments with air-borne SARs as well as in Seasat and SIR-B hindcast studies. Nevertheless, the routine interpretation and application of SAR wave data is still generally regarded as a major unresolved problem because of the inherent complexities of the basically nonlinear imaging process.

A fundamental difficulty is that not all of the wave spectral information is mapped into the SAR image plane. Since SAR images provide only a snapshot of the instantaneous sea surface, they can determine the wave propagation direction only to within a sign. (The ambiguity can be removed, however, by correlating successive looks of the same scene [cf. Rosenthal *et al.*, 1989; Vachon and Raney, 1989]. A more serious loss of information is incurred by the nonlinear distortion induced by motion effects. These result in an azimuthal high wave number cutoff of the spectrum. The nonlinearities also produce significant shifts of the spectral peak and other distortions of the spectrum [Alpers and Brüning, 1986; Brüning *et al.*, 1988, 1990].

Most of these limitations, if properly understood, can be suitably dealt with if the SAR ocean wave image data are assimilated into a wave model. However, this is feasible only if there exists an accurate, operationally feasible method of computing the SAR image spectrum for a given wave spectrum, together with an associated technique for inverting the mapping relation. An essential first step toward the application of SAR wave data in wave models must therefore be the derivation of an efficient and accurate method for computing the mapping from a surface wave spectrum into a SAR surface image spectrum. Subsequently, a method must be devised for dealing with the loss of information incurred in the forward mapping relation and recovering the wave spectrum from the measured SAR image spectrum. Both of these questions are addressed in this paper.

Since the basic imaging mechanisms are known, a straightforward method of solving the forward mapping problem is to compute the SAR image for any given instantaneous realization of the sea surface pixel-by-pixel for each (moving) scattering element of the surface. Monte Carlo computations of the spectrum of the SAR image for a given two-dimensional wave spectrum using an ensemble of such deterministic mapping computations have been carried out by Alpers [1983], Alpers *et al.* [1986], Alpers and Brüning [1986], Lyzenga [1986], Brüning *et al.* [1988, 1990], and Hasselmann *et al.* [1988]. The transformation of the input wave spectrum into the output SAR image spectrum is determined in this method by generating an ensemble of individual surface wave field realizations for the prescribed surface wave spectrum, computing the image pixel-by-pixel for each realization, carrying out the Fourier transform for each SAR image, and finally forming the SAR image variance spectrum by averaging the modulus squared Fourier amplitudes over the ensemble of realizations.

In this paper we follow an alternative approach to develop a new, closed nonlinear integral mapping relation directly for the spectra. The closed relation circumvents the need for deterministic pixel-by-pixel transformation computations of individual images and is free of the inherent statistical

sampling uncertainty of the "brute force" Monte Carlo approach.

Although the transformation is strongly nonlinear, the notorious closure problem of strongly nonlinear statistical systems does not arise, as the Gaussian property of the input wave field is not affected by the nonlinearities. This enables the expectation values of all higher-order nonlinear functions of the input wave variables occurring in the general relation for the output image spectrum to be reduced to closed expressions of the input wave spectrum.

The final integral transformation relation can be expanded in a Fourier transform series, which can be rapidly evaluated using fast Fourier transform (FFT) algorithms. The expansion also provides useful insights into the contributions to the net imaging process from the separate cross-section modulation and surface motion terms, together with their various interaction combinations.

Finally, with the availability of a closed, noise free, rapidly computable transformation expression, it is now possible to address the inverse problem of deriving the wave spectrum from the SAR spectrum. Because of the loss of information beyond the azimuthal cutoff and the 180° ambiguity, a rigorous inverse mapping solution does not exist. However, regularization can be achieved in the usual manner by minimizing a cost function which penalizes not only the deviation between the observed and predicted SAR spectrum, but also the deviation between the modified wave spectrum and a first-guess wave spectrum. The iterative inversion method developed in this paper generally converges within three or four iterations. The computations should be sufficiently rapid for application in an operational SAR data assimilation system.

The paper is structured as follows: section 2 reviews the different imaging mechanisms and defines notation. The basic nonlinear mapping relation is derived in section 3. Section 4 describes the inversion method. The results of sections 3 and 4 are illustrated in section 5 for three selected SAR images from Seasat, taking as first-guess input spectra the wave spectra derived from a global wave hindcast using the WAM third generation wave model [WAMDIG, 1988]. Section 6, finally, summarizes the principal results and conclusions of the study. An appendix describes the generalization of the pure velocity bunching theory presented in section 3 to higher order processes such as acceleration smearing.

## 2. SAR IMAGING OF OCEAN WAVES

After many years of debate, a rather wide consensus has emerged regarding the principal mechanisms governing the imaging of a moving ocean wave surface by a SAR (cf. MSR). The backscattered return may be represented generally as a superposition of the statistically phase uncorrelated returns from a continuous ensemble of small-scale backscattering surface elements. Although open questions still remain regarding finer details of the backscattering mechanism, it is generally agreed that in the range of incidence angles between 20° and 60° typical for satellite and most research aircraft SAR operations, the backscattered return from each surface element (facet) is dominated by Bragg scattering from short ripple waves. The ripple waves in turn are modulated in their orientation, energy, and motion by longer waves, thereby enabling the SAR to image normal wind-generated ocean waves.

The three basic modulation processes arise through (1) the change in the local incidence angle (tilt) of the facet through the long wave slope, (2) the hydrodynamic interaction between short and long waves, which modulates the energy and wave number of the short Bragg scattering waves, and (3) the advection of the backscattering facet by the long wave orbital velocity, which produces a Doppler shift in the return signal and induces an azimuthal displacement of the scattering element in the image plane.

For all processes, it can be assumed that to first order the backscattering ripple waves and the modulating ocean waves are widely separated in wavelength scale. On the basis of this two-scale description, a rather complete theory of SAR imaging of a random ocean wave field can be developed [Alpers and Rufenach, 1979; Swift and Wilson, 1979; Valenzuela, 1980; Alpers et al., 1981; Raney, 1981; Tucker, 1985; MSR].

An important feature of the theory is that SAR imaging is typically nonlinear. Although the hydrodynamic and tilt modulation can usually be approximated as linear processes, the so called velocity bunching mechanism associated with the orbital motion of the long waves is frequently strongly nonlinear, particularly for wind seas and short waves. Velocity bunching arises through the variations in the azimuthal displacements of the imaged backscattering elements induced by the variations of the orbital velocity within the long wave field. The alternate bunching and stretching of the apparent scatterer distribution in the image plane produces an image of the long waves, even in the hypothetical case that the backscattering cross section itself is not modulated. When the displacements are small compared with the characteristic wavelength of the long waves, the mechanism can be treated as a linear process, characterized by a velocity bunching modulation transfer function (MTF), in analogy with the hydrodynamic and tilt MTFs. For larger displacements, however, the process becomes nonlinear, and when the displacements significantly exceed a wavelength (for example, for short wind waves traveling in the azimuthal direction), the image can become completely smeared out.

Since the velocity bunching nonlinearity normally strongly dominates over any nonlinearities of the tilt or hydrodynamic modulation, we shall simply ignore the latter to avoid unnecessarily complicating the analysis, although higher order tilt and hydrodynamic modulation terms (to the extent that they are known) can in principle be readily included [cf. Hasselmann et al., 1990].

In the following it will be convenient to regard the SAR wave image as produced by two consecutive imaging processes: the frozen surface (or real aperture radar, RAR) imaging mechanism, governed by the hydrodynamic and tilt modulation, and the additional motion effects, which are specific to a SAR and do not affect the RAR image.

#### The Frozen Surface Contribution

In the framework of linear modulation theory, the surface elevation  $\zeta(\mathbf{r}, t)$  and the variations of the local (specific) backscattering cross section  $\sigma(\mathbf{r}, t)$  sensed by a RAR may both be represented as a superposition of propagating wave components,

$$\zeta(\mathbf{r}, t) = \sum_{\mathbf{k}} \zeta_{\mathbf{k}} \exp(i[\mathbf{k} \cdot \mathbf{r} - \omega t]) + \text{complex conjugate} \quad (1)$$

$$\sigma(\mathbf{r}, t) = \bar{\sigma} \left\{ 1 + \left[ \sum_{\mathbf{k}} m_{\mathbf{k}} \exp i(\mathbf{k} \cdot \mathbf{r} - \omega t) + \text{c.c.} \right] \right\} \quad (2)$$

where  $\bar{\sigma}$  denotes the spatially averaged specific cross section,  $\omega = (gk)^{1/2}$  is the gravity wave frequency, and the cross-section modulation factor  $m_{\mathbf{k}}$  and wave amplitude  $\zeta_{\mathbf{k}}$  are linearly related through the RAR modulation transfer function  $T_{\mathbf{k}}^R$ ,

$$m_{\mathbf{k}} = T_{\mathbf{k}}^R \zeta_{\mathbf{k}} \quad (3)$$

(Note that the MTFs refer here to the wave height components,  $\zeta_{\mathbf{k}}$  and not, as often defined, to the wave slope  $|\mathbf{k}| \zeta_{\mathbf{k}}$ .)

A discrete Fourier sum notation has been chosen rather than continuous Fourier, or more rigorously, Fourier-Stieltjes, integrals, as we shall be considering later derivatives with respect to individual Fourier components. The discrete representation avoids the rather cumbersome functional derivative notation required for continuous integrals. The transition to continuous integrals is carried out at the end of the analysis.

For the general theory presented in the next section,  $T_{\mathbf{k}}^R$  need not be further specified. However, for later numerical applications,  $T_{\mathbf{k}}^R$  needs to be evaluated in more detail by decomposition into its tilt and hydrodynamic modulation components,

$$T_{\mathbf{k}}^R = T_{\mathbf{k}}^t + T_{\mathbf{k}}^h \quad (4)$$

For a Phillips  $k^{-4}$  high wave number spectrum, the tilt MTF can be approximated for large dielectric constants (which for seawater are of the order of 80), by the expressions [cf. Wright, 1968; Lyzenga, 1986]

$$T^t(\mathbf{k}) = 4ik_l \cot \theta (1 + \sin^2 \theta)^{-1} \quad \theta \leq 60^\circ \quad (5)$$

$$T^h(\mathbf{k}) = 8ik_l (\sin 2\theta)^{-1}$$

for vertical polarization (VV) and for horizontal polarization (HH), respectively, where  $\theta$  is the radar incidence angle and  $k_l$  the component of the incident wave number vector in the radar look direction.

The hydrodynamic MTF can be derived from a two-scale model of hydrodynamic short wave-long wave interactions. A simple relaxation type source term, characterized by a damping factor  $\mu$ , is normally introduced to describe the response of the short waves to the long wave modulation [cf. Keller and Wright, 1975]. Feindt [1985] found that a better agreement with laboratory measurements could be obtained by including an additional feedback term, characterized by a complex feedback factor  $Y_r + iY_i$ , representing the long wave modulation of the wind input to the short waves. This yields a hydrodynamic MTF

$$T_{\mathbf{k}}^h = \frac{\omega - i\mu}{\omega^2 + \mu^2} (4.5)k\omega \left( \frac{k_y^2}{k^2} + Y_r + iY_i \right) \quad (6)$$

Coordinates are chosen such that the  $x$  axis points in the SAR flight (azimuthal) direction and the  $y$  axis forms a right-handed coordinate system with  $x$  (thus  $y$  points in the positive or negative look direction  $l$  for a left or right looking SAR, respectively).

To first order, both RARs and SARs produce quasi-instantaneous images of the surface at a fixed time,  $t = 0$ ,

say. We shall ignore for simplicity the distortion effects due to the fact that a side looking radar does not, in fact, take an instantaneous snapshot but builds up an image from a sequence of consecutively imaged range strips. Thus, moving waves are imaged with slightly Doppler displaced "wave numbers of encounter." This straightforward geometric effect applies equally for a RAR and a SAR and should be distinguished from the SAR motion effects summarized in the following subsection. It can be important for more slowly moving aircraft SARs but is generally negligible for spaceborne SAR imagery. In the same spirit, we shall ignore effects arising from the time delay between individual images in multilook images, which can be used, for example, to gain information on the wave propagation direction, as mentioned above.

Since both RARs and SARs produce quasi-instantaneous images of the surface at time  $t = 0$ , say, the Fourier decomposition of the image modulation intensity  $I(\mathbf{r})$  (after subtraction of the mean) has the form

$$I(\mathbf{r}) = \sum_{\mathbf{k}} I_{\mathbf{k}} \exp(i\mathbf{k} \cdot \mathbf{r}) \quad (7)$$

where

$$I_{\mathbf{k}} = (I_{-\mathbf{k}})^* \quad (8)$$

The structural difference between the Fourier representations (1), (2), and (7) is sometimes overlooked. In contrast to the standard two-dimensional Fourier form (7), equations (1) and (2) really represent three-dimensional wave number-frequency spectra. They can be represented as two-dimensional distributions, however, because the frequencies are constrained to lie on the two free gravity wave dispersion surfaces  $\omega = \pm\sqrt{gk}$ . Thus in (1) and (2) Fourier components of opposite sign in  $\mathbf{k}$  represent different waves traveling in opposite directions, and are not related, in contrast to (7), where the components are related through (8). (For the same reason, (1) and (2) include a second explicit complex conjugate sum, whereas in (7) the complex conjugate wave number pairs are already included implicitly in the single sum over positive and negative  $\mathbf{k}$ .)

For a RAR, the image intensity is directly proportional to the specific cross section. Thus if the image modulation is normalized by the mean image intensity, we have

$$I^R(\mathbf{r}) \equiv \sigma(\mathbf{r}, 0)/\bar{\sigma} - 1 \quad (9)$$

and (1)–(3), (7), and (8) yield

$$I_{\mathbf{k}}^R = T_{\mathbf{k}}^R \zeta_{\mathbf{k}} + (T_{-\mathbf{k}}^R \zeta_{-\mathbf{k}})^* \quad (10)$$

We have not explicitly introduced the RAR (SAR) system transfer function into (9) and (10). This may be represented simply as an additional multiplicative factor in the right-hand side of (10). We shall assume in the following that the system transfer function has already been incorporated in the definition of  $T_{\mathbf{k}}^R$ .

We have also not considered clutter effects. To first order, these may be represented simply as an additional clutter noise spectrum superimposed on the image spectrum considered here [cf. *Alpers and Hasselmann, 1982*].

In terms of the ocean wave and RAR image variance spectra  $F_{\mathbf{k}}$ ,  $P_{\mathbf{k}}^R$ , defined by

$$\langle \zeta^2 \rangle = \sum_{\mathbf{k}} F_{\mathbf{k}} = 2 \sum_{\mathbf{k}} \langle \zeta_{\mathbf{k}}^* \zeta_{\mathbf{k}} \rangle \quad (11)$$

$$\langle I^R{}^2 \rangle = \sum_{\mathbf{k}} P_{\mathbf{k}}^R = \sum_{\mathbf{k}} \langle I_{\mathbf{k}}^R{}^* I_{\mathbf{k}}^R \rangle \quad (12)$$

where the angle brackets denote ensemble means, the linear relation (10) yields

$$P_{\mathbf{k}}^R = \frac{1}{2} \{ |T_{\mathbf{k}}^R|^2 F_{\mathbf{k}} + |T_{-\mathbf{k}}^R|^2 F_{-\mathbf{k}} \} \quad (13)$$

### Motion Effects

We consider now the modification of the frozen image induced by the surface motion. This is normally described by two effects: the azimuthal displacement  $\xi$  of the apparent position of a backscattering element in the image plane, and an azimuthal smearing or broadening  $\Delta x$  of the image of the (theoretically infinitesimal) backscattering element.

According to standard SAR imaging theory, the azimuthal displacement  $\xi$  of the backscattering element is proportional to the range component  $v$  of the long wave orbital velocity with which the backscattering element is advected,

$$\xi = \beta v \quad (14)$$

where

$$\beta = (\text{slant range } \rho)/(\text{SAR platform velocity } U) \quad (15)$$

The orbital velocity  $v$  is defined here as the time average over the period during which the scattering element is viewed by the SAR. Normally, the SAR illumination time is small compared with the wave period, so that to first order,  $v$  may be set equal to the instantaneous orbital velocity in the center of the viewing window.

From classical surface wave theory [*Lamb, 1932*],

$$v = \sum_{\mathbf{k}} T_{\mathbf{k}}^v \zeta_{\mathbf{k}} \exp(i\mathbf{k}\mathbf{r}) + \text{c.c.} \quad (16)$$

where the range velocity transfer function is given by

$$T_{\mathbf{k}}^v = -\omega \left( \sin \theta \frac{k_l}{|k|} + i \cos \theta \right) \quad (17)$$

We have neglected for simplicity the small additional Doppler shift due to the finite phase velocity of the Bragg scattering ripples. This can be readily included in the theory but encumbers the notation. We shall also neglect the Doppler shifts due to the dynamics of the ripple waves, which are smaller than the phase velocity terms by another order of magnitude, and would appear formally in a smearing term (cf. MSR).

The smearing term  $\Delta x$  is normally represented as the sum of a second-order acceleration term and a velocity spread term (cf. MSR).

The acceleration smearing arises through the variation of the instantaneous orbital velocity during the SAR viewing interval. This yields slightly different effective displacements  $\xi$  for the beginning and end of the SAR illumination period. The term is generally an order of magnitude smaller than the velocity spread term [cf. *Alpers and Rufenach, 1979*; *Alpers et al., 1981*; MSR]. To simplify the presentation, it will not

be considered in this section. However, the extension of the theory to include this effect is basically straightforward and is presented in the appendix.

The velocity spread term is identical in physical origin to the azimuthal displacement term. It is generally introduced as a separate term primarily for conceptual purposes [cf. *Tucker, 1985; MSR*], although the distinction also has important practical implications for Monte Carlo simulations. In the present theory, however, there is no need to treat the velocity spread term separately from the general velocity bunching formalism. The term has nevertheless played some role in the discussion of the azimuthal cutoff of SAR images, which will be considered in the following section, and is therefore briefly described here.

The velocity spread term arises through the introduction of a second separation scale, the SAR resolution scale  $L_{\text{SAR}}$ , into the SAR imaging model. The scale  $L_{\text{SAR}}$  is typically of order 20 m and is therefore an order of magnitude larger than the basic separation scale  $L_{\text{hyd}}$  of the standard hydrodynamic interaction and Bragg backscattering two-scale model. The scale  $L_{\text{hyd}}$  lies between the wavelength of the Bragg scattering ripples and the long waves and is thus generally of order 1 m. Since the SAR is unable to distinguish between individual backscattering facets within a SAR resolution cell, the entire ensemble of backscattering facets within a resolution cell is mapped into a single image pixel. The mean azimuthal displacement of the pixel is given by  $\bar{\xi} = \beta\bar{v}$ , where  $\bar{v}$  is the mean orbital velocity of the cell facet ensemble. The deviations  $\xi - \bar{\xi}$  of the individual facet displacements relative to this mean value then produce the ‘‘velocity spread’’ smearing of the image of the resolution cell.

In Monte Carlo simulations, this subresolution smearing can be treated as a statistical process which can be represented simply as an effective degradation of the SAR system MTF. The long wave spectrum can then be subdivided at the scale  $L_{\text{SAR}}$ , and only waves with scales greater than  $L_{\text{SAR}}$  need be included explicitly in the simulation. The mapping computations can therefore be carried out at the relatively coarse resolution of the SAR rather than at the much finer resolution scale  $L_{\text{hyd}}$  of the backscattering facets.

In the present analysis, however, the subdivision of the wave spectrum at the SAR separation scale  $L_{\text{SAR}}$  is unnecessary, since the theory can be carried through uniformly up to the high wave number cutoff  $(L_{\text{hyd}})^{-1}$  of the backscattering-hydrodynamic two-scale model. We may therefore regard the SAR image directly as the superposition of the (statistically independent) images of all subresolution scale backscattering facets, without clustering these elements together to larger entities of the dimension of the SAR resolution cell.

The relation between the SAR and RAR images in the present ‘‘pure velocity bunching’’ model is obtained by simply mapping each facet at position  $\mathbf{r}'$  into its corresponding position  $\mathbf{r} = \mathbf{r}' + \xi(\mathbf{r}')$  in the image plane,

$$\hat{I}^S(\mathbf{r}) = \int \hat{I}^R(\mathbf{r}') \delta[\mathbf{r} - \mathbf{r}' - \xi(\mathbf{r}')] d\mathbf{r}' \quad (18)$$

where  $\xi = a\xi$ ,  $\mathbf{a}$  denotes the unit vector in the azimuthal ( $x$ ) direction, and

$$\hat{I}^{S,R}(\mathbf{r}) = 1 + I^{S,R}(\mathbf{r}) \quad (19)$$

is the total normalized image intensity.

Integrating out the  $\delta$  function, (18) yields

$$\hat{I}^S(\mathbf{r}) = \left\{ \hat{I}^R(\mathbf{r}') \left| \frac{d\mathbf{r}'}{d\mathbf{r}} \right| \right\}_{\mathbf{r}' = \mathbf{r} - \xi(\mathbf{r}')} \quad (20)$$

The Jacobian velocity bunching factor

$$\left| \frac{d\mathbf{r}'}{d\mathbf{r}} \right| = \left| 1 + \frac{d\xi'(\mathbf{r}')}{d\mathbf{r}'} \right|^{-1} \quad (21)$$

represents the variation in the effective density of backscattering elements in the image plane due to the compression or stretching of the originally homogeneous distribution of facets. As pointed out, this enables the SAR to image ocean waves even in the hypothetical situation in which the RAR transfer function vanishes, i.e.,  $I^R(\mathbf{r}) = 0$ .

For the case

$$\left| \frac{\partial \xi'}{\partial \mathbf{r}'} \right| \ll 1 \quad (22)$$

(21) can be expanded in a power series and truncated after the linear term. Equations (20) and (21) yield then for the SAR image amplitude spectrum, applying (14) and (16),

$$I_{\mathbf{k}}^S = I_{\mathbf{k}}^R + [T_{\mathbf{k}}^{vb} \zeta_{\mathbf{k}} + (T_{-\mathbf{k}}^{vb} \zeta_{-\mathbf{k}})^*] \quad (23)$$

where the velocity bunching modulation transfer function

$$\begin{aligned} T_{\mathbf{k}}^{vb} &= -i\beta k_x T_{\mathbf{k}}^v \\ &= -\beta k_x \omega (\cos \theta - i \sin \theta k_x/k) \end{aligned} \quad (24)$$

Thus in the linear approximation

$$I_{\mathbf{k}}^S = T_{\mathbf{k}}^S \zeta_{\mathbf{k}} + (T_{-\mathbf{k}}^S \zeta_{-\mathbf{k}})^* \quad (25)$$

and the image variance spectrum is given by

$$P_{\mathbf{k}}^S = |T_{\mathbf{k}}^S|^2 \frac{F_{\mathbf{k}}}{2} + |T_{-\mathbf{k}}^S|^2 \frac{F_{-\mathbf{k}}}{2} \quad (26)$$

with the net SAR imaging modulation transfer function

$$T_{\mathbf{k}}^S = T_{\mathbf{k}}^R + T_{\mathbf{k}}^{vb} \quad (27)$$

The condition (22) is generally satisfied for swell. However, in many situations, in particular for short wind seas, the inequality does not hold or is even reversed [cf. *MSR; Brüning et al., 1990*]. Moreover, even for sea states for which (22) applies in a spectrally averaged sense, the inequality breaks down for short azimuthally propagating waves. Thus in all cases, (18) and (20) represent a strongly nonlinear transformation either for all or at least part of the spectrum, and we must address the general problem of deriving the fully nonlinear transformation relation between the surface wave spectrum and the SAR image spectrum.

### 3. GENERAL NONLINEAR MAPPING RELATION

To determine the dependence of the SAR image Fourier components  $I_{\mathbf{k}}^S$  on the wave Fourier components in the general nonlinear case, we first apply a Fourier transform to the basic mapping relation (20):

$$I_{\mathbf{k}}^S = \frac{1}{A} \int d\mathbf{r} \exp(-i\mathbf{k} \cdot \mathbf{r}) \left\{ \hat{I}^R(\mathbf{r}') \left| \frac{d\mathbf{r}'}{d\mathbf{r}} \right| \right\}_{\mathbf{r}' = \mathbf{r} - \xi(\mathbf{r})}$$

$$= \frac{1}{A} \int d\mathbf{r}' \hat{I}^R(\mathbf{r}') \exp\{-i\mathbf{k} \cdot [\mathbf{r}' + \xi(\mathbf{r}')]\} \quad (28)$$

Here  $A$  denotes the finite rectangular area of the sea surface corresponding to the discrete Fourier representation (in the final expression,  $A \rightarrow \infty$ ).

Substituting the Fourier representation (7), (10) for  $I^R$  into (28), we obtain

$$I_{\mathbf{k}}^S = \frac{1}{A} \int d\mathbf{r}' \left\{ 1 + \sum_{\mathbf{k}'} (T_{\mathbf{k}'}^R \zeta_{\mathbf{k}'} + T_{-\mathbf{k}'}^{R*} \zeta_{-\mathbf{k}'}^*) \right. \\ \left. \cdot \exp i\mathbf{k}' \cdot \mathbf{r}' \right\} \exp[-i\mathbf{k} \cdot \mathbf{r}' - i\mathbf{k} \cdot \xi(\mathbf{r}')] \quad (29)$$

This yields for the SAR image variance spectrum

$$P_{\mathbf{k}}^S = \langle I_{\mathbf{k}}^S \cdot (I_{\mathbf{k}}^S)^* \rangle \\ = \left\langle A^{-2} \iint d\mathbf{r}' d\mathbf{r}'' \right. \\ \left. \cdot \exp\{-i\mathbf{k} \cdot (\mathbf{r}' - \mathbf{r}'') - i\mathbf{k} \cdot [\xi(\mathbf{r}') - \xi(\mathbf{r}'')]\} \right. \\ \left. \cdot \left\{ 1 + \sum_{\mathbf{k}'} (T_{\mathbf{k}'}^R \zeta_{\mathbf{k}'} + T_{-\mathbf{k}'}^{R*} \zeta_{-\mathbf{k}'}^*) e^{i\mathbf{k}' \cdot \mathbf{r}'} \right\} \right. \\ \left. \cdot \left\{ 1 + \sum_{\mathbf{k}''} (T_{\mathbf{k}''}^{R*} \zeta_{\mathbf{k}''}^* + T_{-\mathbf{k}''}^R \zeta_{-\mathbf{k}''}) e^{-i\mathbf{k}'' \cdot \mathbf{r}''} \right\} \right\rangle \quad (30)$$

The nonlinearity of this integral expression appears solely in the factor

$$N_{\mathbf{k}} = \exp\{-i\mathbf{k} \cdot [\xi(\mathbf{r}') - \xi(\mathbf{r}'')]\} \quad (31)$$

The term occurs in the following mean product combinations:

$$E_{\mathbf{k}'}^a = \langle N_{\mathbf{k}'} \cdot \zeta_{\mathbf{k}'} \rangle \quad E_{\mathbf{k}'}^b = \langle N_{\mathbf{k}'} \cdot \zeta_{-\mathbf{k}'}^* \rangle \quad (32)$$

$$E_{\mathbf{k}'\mathbf{k}''}^{aa} = \langle N_{\mathbf{k}'} \cdot \zeta_{\mathbf{k}'} \zeta_{\mathbf{k}''} \rangle \quad E_{\mathbf{k}'\mathbf{k}''}^{ab} = \langle N_{\mathbf{k}'} \cdot \zeta_{\mathbf{k}'} \zeta_{-\mathbf{k}''}^* \rangle \quad (33)$$

$$E_{\mathbf{k}'\mathbf{k}''}^{ba} = \langle N_{\mathbf{k}'} \cdot \zeta_{-\mathbf{k}'}^* \zeta_{\mathbf{k}''} \rangle \quad E_{\mathbf{k}'\mathbf{k}''}^{bb} = \langle N_{\mathbf{k}'} \cdot \zeta_{-\mathbf{k}'}^* \zeta_{-\mathbf{k}''}^* \rangle \quad (34)$$

To evaluate these expressions, we decompose  $N_{\mathbf{k}}$  into a sum over a set of terms each of which is composed of two statistically independent factors. The first factor consists of an infinitesimal expression containing the specific wave components which appear in the products (32)–(34). The second factor contains the remaining components of the wave field. Since for a Gaussian wave field all wave components are statistically independent, the second factor in each term is statistically independent of the first factor, and the mean products (32)–(34) can therefore be immediately evaluated.

The Fourier representation of the azimuthal displacement difference

$$\Delta\xi = \xi(\mathbf{r}') - \xi(\mathbf{r}'') \quad (35)$$

appearing in the exponent of  $N_{\mathbf{k}}$  may be written in the form

$$\Delta\xi = \sum_{\mathbf{k}''} (K_{\mathbf{k}''} \zeta_{\mathbf{k}''} + \text{c.c.}) \quad (36)$$

where

$$K_{\mathbf{k}''} = \beta T_{\mathbf{k}''}^v (e^{i\mathbf{k}'' \cdot \mathbf{r}'} - e^{i\mathbf{k}'' \cdot \mathbf{r}''}) \quad (37)$$

(cf. (14), (16)). Splitting off from the sum (36) the subset  $S$  of infinitesimal wave components which appear in the products (32)–(34), and denoting the residual sum  $\Sigma'$  by  $R$ , we have

$$\Delta\xi = (K_{\mathbf{k}'}^* \zeta_{\mathbf{k}'}^* + K_{\mathbf{k}''}^* \zeta_{\mathbf{k}''}^* + K_{-\mathbf{k}'} \xi_{-\mathbf{k}'} + K_{-\mathbf{k}''} \zeta_{\mathbf{k}''} + \text{c.c.}) \\ + \sum_{\mathbf{k}''} (K_{\mathbf{k}''} \zeta_{\mathbf{k}''} + \text{c.c.}) \\ = S + R \quad (38)$$

Since  $S$  is infinitesimal, we may expand  $N_{\mathbf{k}} = \exp(-i\mathbf{k}_x \Delta\xi)$  in a Taylor series

$$N_{\mathbf{k}} = e^{-i\mathbf{k}_x R} \left( 1 - i\mathbf{k}_x S - k_x^2 \frac{S^2}{2} + \dots \right) \quad (39)$$

The rest sum  $R$  contains only wave components which are statistically independent of the wave component factors  $X$  appearing in (32)–(34). Thus the expectation values in these expressions may be factorized in the form

$$\langle N_{\mathbf{k}} \cdot X \rangle = \langle e^{-i\mathbf{k}_x R} \rangle \left( \langle X \rangle - i\mathbf{k}_x \langle SX \rangle - k_x^2 \frac{\langle S^2 X \rangle}{2} \right) \quad (40)$$

The first term  $\langle X \rangle$  in (40) vanishes, since  $\langle \zeta_{\mathbf{k}} \rangle = 0$ ,  $\langle \zeta_{\mathbf{k}} \zeta_{\mathbf{k}''} \rangle = 0$ ,  $\langle \zeta_{\mathbf{k}} \zeta_{-\mathbf{k}''}^* \rangle = 0$  (except for the subset  $\mathbf{k}' + \mathbf{k}'' = 0$ , which has zero integral measure in the limit of a continuous spectrum). The second term  $\langle SX \rangle$  is proportional to the wave spectrum, while the third term  $\langle S^2 X \rangle$  represents a quadratic wave spectral product. Since  $X$  is either linear (32) or quadratic ((33) and (34)), only the first two terms in the expansion (39) contribute to (40). (In the general theory including acceleration smearing presented in the appendix, however, the full expansion (39) is needed.)

The first factor  $\langle e^{-i\mathbf{k}_x R} \rangle$  in (40) may now be replaced again by  $\langle N_{\mathbf{k}} \rangle$ , since the two expressions differ only by the negligible infinitesimal components  $S$ . The term can be evaluated by again making use of the Gaussian property of the wave field. Since  $\Delta\xi$  is a linear function of the wave field, the variable is normally distributed, and one obtains by direct integration over the probability distribution

$$\langle N_{\mathbf{k}} \rangle = \langle \exp(-i\mathbf{k}_x \Delta\xi) \rangle = \exp(-k_x^2 \langle \Delta\xi^2 \rangle / 2) \quad (41)$$

From (36), we have further

$$\langle \Delta\xi^2 \rangle = 2\beta^2 \int |T_{\mathbf{k}}^v|^2 F(\mathbf{k}) [1 - \cos \mathbf{k}(\mathbf{r}' - \mathbf{r}'')] d\mathbf{k} \\ = 2\xi'^2 [1 - \langle v^2 \rangle^{-1} f^v(\mathbf{r}' - \mathbf{r}'')] \quad (42)$$

where

$$f^v(\mathbf{r}) = \langle v(\mathbf{x} + \mathbf{r})v(\mathbf{x}) \rangle = \int F(\mathbf{k}) |T_{\mathbf{k}}^v|^2 e^{i\mathbf{k} \cdot \mathbf{r}} d\mathbf{k} \quad (43)$$

is the orbital velocity covariance function and

$$\xi'^2 = \langle \xi^2 \rangle = \beta^2 \langle v^2 \rangle = \beta^2 \int |T_{\mathbf{k}}^v|^2 F(\mathbf{k}) d\mathbf{k} \quad (44)$$

is the mean square azimuthal displacement of a scattering element. We have introduced at this point the continuous spectral notation

$$F(\mathbf{k}) = \frac{F_{\mathbf{k}}}{\Delta \mathbf{k}} = (2\pi)^{-2} A F_{\mathbf{k}} \quad (45)$$

After some straightforward algebra to evaluate the mean products within the parentheses in (40), equation (30) yields, together with (42)–(44), the closed nonlinear spectral transform expression

$$\begin{aligned} P^S(\mathbf{k}) &= (2\pi)^{-2} \exp[-k_x^2 \xi'^2] \\ &\cdot \int d\mathbf{r} e^{-i\mathbf{k} \cdot \mathbf{r}} \exp[k_x^2 \xi'^2 \langle v^2 \rangle^{-1} f^v(\mathbf{r})] \\ &\times \{1 + f^R(\mathbf{r}) + ik_x \beta [f^{Rv}(\mathbf{r}) - f^{Rv}(-\mathbf{r})] \\ &+ (k_x \beta)^2 [f^{Rv}(\mathbf{r}) - f^{Rv}(0)][f^{Rv}(-\mathbf{r}) - f^{Rv}(0)]\} \end{aligned} \quad (46)$$

where  $P^S(\mathbf{k}) = P_{\mathbf{k}}^S / \Delta \mathbf{k}$  and

$$\begin{aligned} f^R(\mathbf{r}) &= \langle I^R(\mathbf{x} + \mathbf{r}) I^R(\mathbf{x}) \rangle \\ &= \frac{1}{2} \int \{F(\mathbf{k}) |T_{\mathbf{k}}^R|^2 + F(-\mathbf{k}) |T_{-\mathbf{k}}^R|^2\} e^{i\mathbf{k} \cdot \mathbf{r}} d\mathbf{k} \end{aligned} \quad (47)$$

$$\begin{aligned} f^{Rv}(\mathbf{r}) &= \langle I^R(\mathbf{x} + \mathbf{r}) v(\mathbf{x}) \rangle \\ &= \frac{1}{2} \int \{F(\mathbf{k}) T_{\mathbf{k}}^R (T_{\mathbf{k}}^v)^* + F(-\mathbf{k}) (T_{-\mathbf{k}}^R)^* T_{-\mathbf{k}}^v\} e^{i\mathbf{k} \cdot \mathbf{r}} d\mathbf{k} \end{aligned} \quad (48)$$

represent the autocovariance function of the RAR image intensity  $I^R(\mathbf{x})$  and the covariance function of  $I^R(\mathbf{x})$  and  $v(\mathbf{x})$ , respectively.

Apart from the second exponential factor, the integral (46) has the form of a Fourier transform. It can be reduced to a series of Fourier transforms by expanding the exponential in a Taylor series,

$$\begin{aligned} \exp[k_x^2 \xi'^2 \langle v^2 \rangle^{-1} f^v(\mathbf{r})] \\ = [1 + k_x^2 \xi'^2 \langle v^2 \rangle^{-1} f^v(\mathbf{r}) + \dots] \end{aligned} \quad (49)$$

This yields a spectral series expansion of the form

$$P^S(\mathbf{k}) = \exp(-k_x^2 \xi'^2) \sum_{n=1}^{\infty} \sum_{m=2n-2}^{2n} (k_x \beta)^m P_{nm}^S(\mathbf{k}) \quad (50)$$

where the index  $n$  indicates the nonlinearity order with respect to the input wave spectrum and the index  $m$  the order with respect to the velocity bunching parameter  $\beta$  (which is seen to occur always in combination with the azimuthal wave number  $k_x$ ). Explicitly, the spectral expansion terms are given by

$$P_{n,2n}^S = \Omega_n \left\{ \frac{f^v(\mathbf{r})^n}{n!} \right\} \quad (51)$$

$$P_{n,2n-1}^S = \Omega_n \left\{ \frac{i[f^{Rv}(\mathbf{r}) - f^{Rv}(-\mathbf{r})] f^v(\mathbf{r})^{n-1}}{(n-1)!} \right\} \quad (52)$$

$$\begin{aligned} P_{n,2n-2}^S &= \Omega_n \left\{ \frac{1}{(n-1)!} f^R(\mathbf{r}) f^v(\mathbf{r})^{n-1} \right. \\ &+ \frac{1}{(n-2)!} [f^{Rv}(\mathbf{r}) - f^{Rv}(0)] \\ &\cdot [f^{Rv}(-\mathbf{r}) - f^{Rv}(0)] f^v(\mathbf{r})^{n-2} \end{aligned} \quad (53)$$

where  $\Omega_n$  is the Fourier transform operator

$$\Omega_n = (2\pi)^{-2} \int d\mathbf{r} \exp(-i\mathbf{k} \cdot \mathbf{r}) \quad (54)$$

(for the integers 0, -1 the factorial function is defined as  $0! = 1$  and  $[(-1)!]^{-1} = 0$ ).

We have left out a term  $P_{0,0}$  in the sum representing an irrelevant  $\delta$  function contribution at  $\mathbf{k} = 0$  associated with the mean image intensity.

An expansion with respect to nonlinearity only can be obtained by summing over the velocity bunching index  $m$  for fixed nonlinearity order  $n$ ,

$$\begin{aligned} P^S(\mathbf{k}) &= \exp(-k_x^2 \xi'^2) (P_1^S(\mathbf{k}) + P_2^S(\mathbf{k}) \\ &+ \dots + P_n^S(\mathbf{k}) + \dots) \end{aligned} \quad (55)$$

The linear term  $P_1^S$  is found to be identical (as it must be) with the linear SAR spectrum of (26).

It should be noted that the terms  $P_n^S(\mathbf{k})$  in (55) do not represent the direct expansion of  $P^S(\mathbf{k})$  in powers of the input wave spectrum, as the common (nonlinear) azimuthal cutoff factor  $\exp(-k_x^2 \xi'^2)$  has been taken out of the sum. This is an important feature of the theory.

The first term in the expansion (55) yields the quasi-linear approximation

$$P_{ql}^S(\mathbf{k}) = \exp(-k_x^2 \xi'^2) P_1^S(\mathbf{k}) \quad (56)$$

The significance of the azimuthal cutoff factor is well illustrated by this term. The approximation  $P_1^S(\mathbf{k})$  of purely linear SAR imaging theory, without the cutoff factor, always breaks down for high azimuthal wave numbers, even for very low waves, since real wave spectra (and therefore also the computed linear SAR image spectra) fall off as a power law at high wave numbers, rather than exponentially, as required by (55). In contrast, the lowest order quasi-linear approximation, including the azimuthal cutoff factor, represents a uniformly valid approximation for the entire spectrum.

In a hindcast study of 34 Seasat SAR spectra covering a wide variety of sea states (C. Brüning et al., manuscript in preparation, 1991), it was found that the quasi-linear form (56) yielded an acceptable first-order description of the SAR spectrum for about half of the cases analyzed and captured the qualitative features of the spectrum (although with displaced peaks, etc.) in all cases. The robustness of the quasi-linear approximation will be used in the next section to develop an iterative scheme for inverting the fully nonlinear transformation (55).

The decomposition of the quasi-linear spectrum  $P_{ql}^S$  into its contributions of different velocity bunching order yields

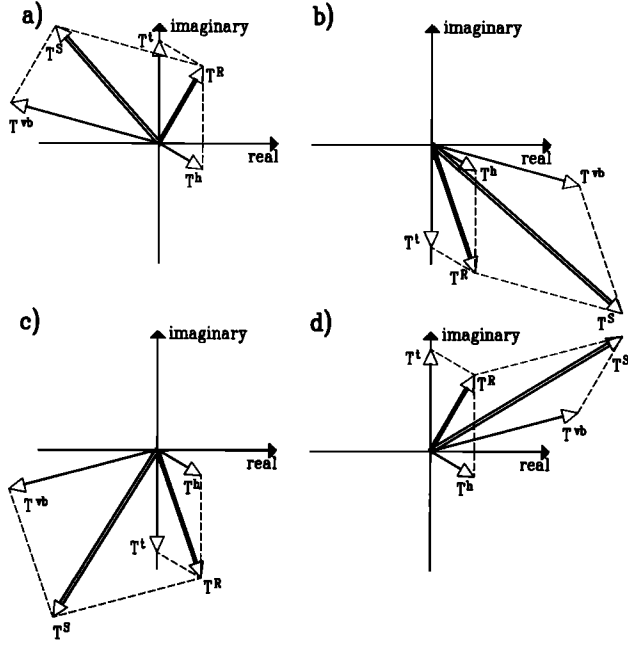


Fig. 1. Orientations of the tilt, hydrodynamic, velocity bunching, and net RAR and SAR MTFs in the complex plane for a given wave component and different sign combinations of the SAR flight and look directions: (a)  $k_x > 0$ ,  $k_y > 0$ ,  $k_l > 0$  (left looking SAR); (b) change in sign of flight direction ( $k_x < 0$ ,  $k_y < 0$ ,  $k_l < 0$ ); (c, d) same as Figures 1a and 1b for a right looking SAR ( $k_l = -k_y$ ).

$$P_{ql}^S = P_{ql}^R + P_{ql}^{int} + P_{ql}^{vb} \quad (57)$$

where the pure RAR spectrum  $P_{ql}^R$ , the pure quasi-linear velocity bunching spectrum  $P_{ql}^{vb}$ , and the quasi-linear interference spectral term  $P_{ql}^{int}$  are given by

$$\begin{Bmatrix} P_{ql}^R \\ P_{ql}^{int} \\ P_{ql}^{vb} \end{Bmatrix} = \exp(-k_x^2 \xi'^2) \begin{Bmatrix} P_{10}^S \\ (k_x \beta) P_{11}^S \\ (k_x \beta)^2 P_{12}^S \end{Bmatrix} \quad (58)$$

Applying (26) and (27), this may be written

$$P_{ql}^{\cdot} = H_k^{\cdot} \cdot \frac{F_k}{2} + H_{-k}^{\cdot} \cdot \frac{F_{-k}}{2} \quad (59)$$

(for any index  $R$ ,  $int$ ,  $vb$ , or  $S$ ), where

$$\begin{Bmatrix} H_k^R \\ H_k^{int} \\ H_k^{vb} \\ H_k^S \end{Bmatrix} = \exp(-k_x \xi'^2) \begin{Bmatrix} |T_k^R|^2 \\ (T_k^R T_k^{vb*} + T_k^{R*} T_k^{vb}) \\ |T_k^{vb}|^2 \\ |T_k^S|^2 \end{Bmatrix} \quad (60)$$

The orientations in the complex plane of the various MTFs which determine the filter factors  $H_k^{\cdot}$  are indicated in Figure 1. The MTFs apply for a given surface wave component and various sign combinations of the SAR look and flight directions. Figure 1a applies to a wave component traveling in the positive quadrant of the  $xy$  plane ( $k_x > 0$ ,  $k_y > 0$ ) and a left looking SAR ( $k_l = k_y$ ). Figure 1b applies for the same left looking SAR viewing the same wave component but for a SAR platform flying in the opposite direction ( $k_x < 0$ ,  $k_y = k_l < 0$ ). Figures 1c and 1d correspond to Figures 1a and 1b, respectively, for a right looking SAR ( $k_l = -k_y$ ). The resultant SAR MTF is seen to

be strongly dependent on the orientation of the SAR look and flight directions. This has been confirmed by aircraft SAR measurements [e.g., Hasselmann *et al.*, 1989].

The strong dependence on the viewing geometry is at first sight perhaps surprising, since the moduli of the individual velocity bunching, tilt, and hydrodynamic transfer functions are invariant with respect to the four viewing combinations shown in Figure 1. The modulus of the net RAR transfer function is also only weakly dependent on the look and flight direction (through the imaginary component of the hydrodynamic MTF, which, in contrast to the imaginary tilt MTF, is invariant with respect to the look and flight direction).

Since the moduli of the separate filter functions  $H_k^R$  and  $H_k^{vb}$  for pure RAR and pure velocity bunching imaging, respectively, are approximately or exactly independent of the sign combinations of the viewing geometry, the strong viewing geometry dependence of the net SAR filter function,

$$H_k^S = H_k^R + H_k^{int} + H_k^{vb} \quad (61)$$

must come about through the interference filter function  $H_k^{int}$ .

This is illustrated by the plots of the four filter functions  $H_k^R$ ,  $H_k^{int}$ ,  $H_k^{vb}$  and  $H_k^S$  shown in Figure 2. The cutoff scale was chosen as  $\xi' = 70$  m, or  $k_x^{cutoff} = (\xi')^{-1} = 0.014 \text{ m}^{-1}$ , corresponding to the Seasat value  $\beta = 113.5$  and a Pierson-Moskowitz [Pierson and Moskowitz, 1964] fully developed wind sea spectrum for a wind speed at 10 m height of 10 m/s ( $(\langle v^2 \rangle)^{1/2} = 0.62 \text{ m/s}$ ). The damping factor in  $T_k^{hyd}$  (equation (6)) was set at  $\mu = 0.5 \text{ s}^{-1}$ , and no wind input modulation terms were included (as in the Seasat computations in section 5).

The filter function  $H_k^{vb}$  is seen to be exactly symmetrical with respect to a change in sign of  $k_x$  or  $k_y$ , the filter function  $H_k^R$  is exactly symmetrical with respect to a change in sign of  $k_x$  and approximately symmetrical with respect to a change in sign of  $k_y$ , while the filter function  $H_k^{int}$  is exactly antisymmetrical with respect to the transformation  $k_y \rightarrow -k_y$ . The net filter function  $H_k^S$  is therefore approximately symmetrical with respect to a change in sign of  $k_y$ , but has pronounced asymmetries with respect to the transformation  $k_x \rightarrow -k_x$ .

The general structures of the filter functions shown in Figure 2 are independent of the parameters chosen. It will be useful to keep Figure 2 in mind later in discussing the origin of the various distortions and asymmetries found in computed and observed SAR image spectra.

As pointed out, the common azimuthal cutoff factor applies not only to the quasi-linear spectral terms but also to the entire series expansion (50) or (55). This has a useful practical implication. The azimuthal cutoff of an observed SAR spectrum is usually a relatively well-defined feature. Its experimental determination, independent of the details of the mapping process, yields an important integral property of the wave spectrum, the mean square orbital velocity (cf. (44)).

Beal *et al.* [1983], Lyzenga [1986], and Monaldo and Lyzenga [1986, 1988] have verified experimentally the proportionality of the azimuthal cutoff scale to the rms orbital range velocity component, or some related integral property of the wave field. Previously, this finding has been difficult to interpret theoretically. The SAR two-scale model using the SAR resolution scale as separation scale yields a cutoff

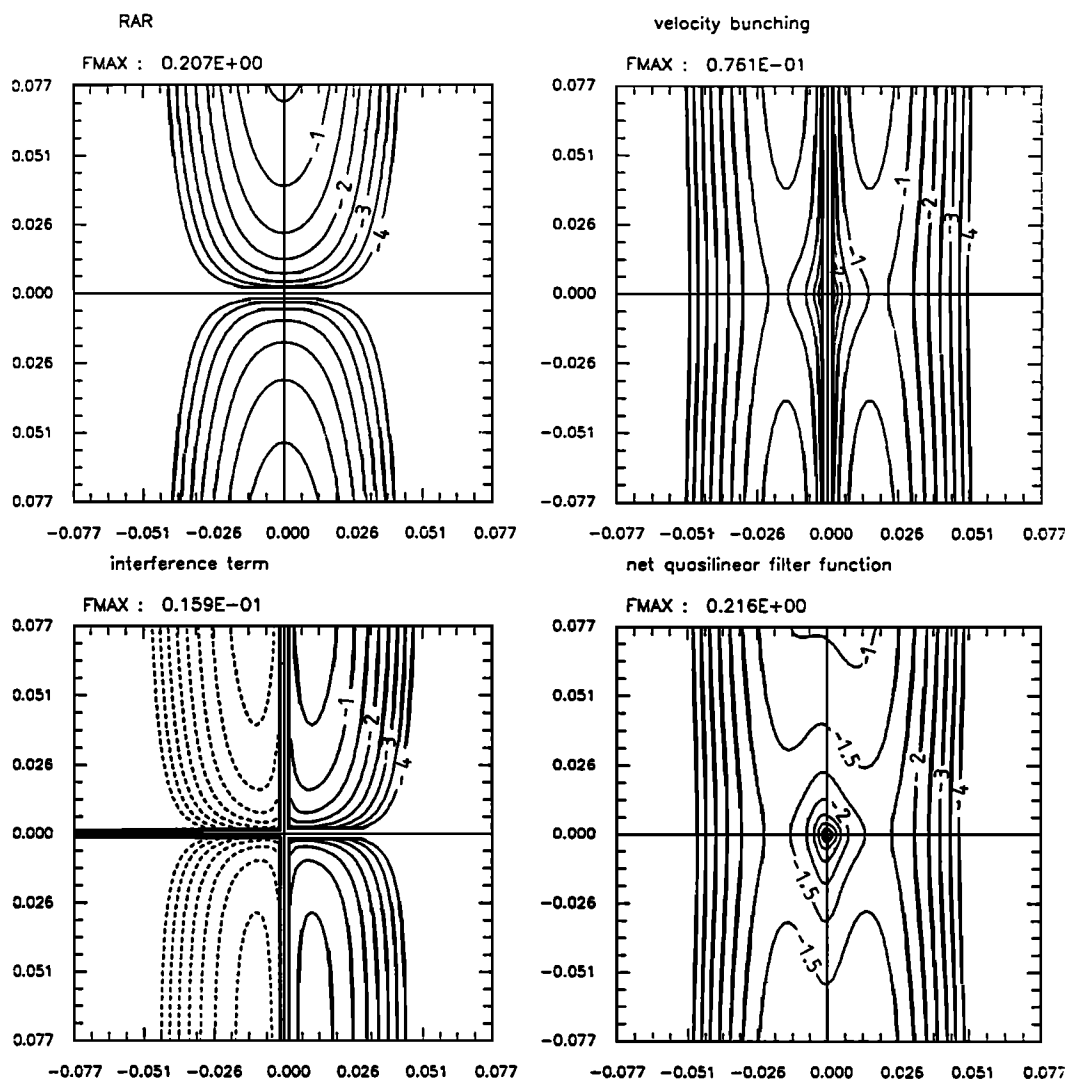


Fig. 2. The quasi-linear spectral filter functions  $H_k^R$ ,  $H_k^{\text{int}}$ ,  $H_k^{vb}$ , and  $H_k^S$ . Note the exact symmetry of  $H_k^{vb}$ , the approximate symmetry of  $H_k^R$ , and the antisymmetry of  $H_k^{\text{int}}$ , yielding a nonsymmetrical net filter function  $H_k^S$ . Isolines are logarithmically spaced relative to the maximum value, with two isolines per decade.

factor due to velocity spreading which is determined by the rms orbital velocity in the subresolution short wave spectral band between the SAR resolution scale and the facet scale. Tucker [1985] computed the contribution of this velocity spread smearing and obtained an azimuthal cutoff factor which was indeed identical to our form, but with  $\zeta'$  replaced by the rms azimuthal displacement (the "velocity spread") of only the short subresolution scale waves. The present closed theory implies that the nonlinear velocity bunching mechanism in the "deterministic" wave number region, below the SAR resolution wave number, not only distorts the spectrum in this region, but must also contribute to the azimuthal cutoff. When this effect is combined with the velocity spread term, one obtains the simple result that the net azimuthal filtering can be represented by a common Gaussian cutoff factor which acts on all terms in the nonlinear spectral expansion.

We conclude this section by summarizing again the basic three computational steps needed to determine the SAR spectrum according to (50):

1. Computation of the three autovariance and covariance functions  $f^v(r)$ ,  $f^R(r)$ , and  $f^{Rv}(r)$  using the Fourier transform relations (43), (47), and (48).
2. Computation of the covariance product expressions appearing in (51)–(53).
3. Computation of the Fourier transforms (51)–(53). If only the final SAR spectrum is of interest, without regard for the separate contributions from different nonlinearity order, the covariance products of different nonlinearity order  $n$  for given velocity bunching order  $m$  (power of  $\beta k_x$ ) can be collected together and Fourier transformed in a single operation.

Since only Fourier transforms are involved, the computations are rather fast (less than 1 s on a CRAY-2, for  $128 \times 128$  pixel scene using full FFT representations). Good convergence was normally attained even for strongly nonlinear spectra with a truncation at nonlinearity order  $n = 6$ . The higher order terms contribute mainly to the resolution of the (normally not very important) details near the azimuthal cutoff (cf. section 5).

## 4. INVERSION

A unique formal inversion of the forward mapping relation cannot exist in view of the 180° ambiguity of the SAR image and the loss of information beyond the azimuthal cutoff. The standard procedure for resolving such underdetermined inversion problems is to introduce a regularization term which makes use of additional information from a first-guess wave spectrum  $\hat{F}(\mathbf{k})$ .

Following this approach, we define the optimal fit wave spectrum  $F(\mathbf{k})$  as the spectrum which minimizes the cost function

$$J = \int [P(\mathbf{k}) - \hat{P}(\mathbf{k})]^2 d\mathbf{k} + \mu \int \left[ \frac{[F(\mathbf{k}) - \hat{F}(\mathbf{k})]^2}{[B + \hat{F}(\mathbf{k})]} \right] d\mathbf{k} \quad (62)$$

where  $\hat{P}(\mathbf{k})$ ,  $P(\mathbf{k})$  are the observed and fitted SAR spectra, respectively (the index  $S$  has been dropped, as there is now no need to distinguish between the SAR and RAR spectrum),  $\mu$  is some suitably chosen weight reflecting the relative confidence ascribed to the observed SAR spectrum and the first-guess wave spectrum (which will normally be provided by a wave model), and a small positive constant  $B$  has been introduced into the normalizing denominator in the second integral to avoid numerical infinities for  $\hat{F}(\mathbf{k}) = 0$  (formally, infinities in normalizing factors are acceptable, as they merely express an infinitely hard side condition).

Equation (62) can be generalized by introducing wave number dependent weights within the integrals or a nondiagonal metric. The rationale for such generalizations is normally provided by maximum likelihood considerations. Since the required input for these generalizations (the error covariance matrix for the combined data set  $\hat{P}(\mathbf{k})$ ,  $\hat{F}(\mathbf{k})$ ) cannot be readily estimated in our case, these options were not further pursued.

However, to enhance the agreement of the computed and observed SAR spectra in the neighborhood of the SAR spectral peaks, we considered also the alternative cost function

$$J' = \int [P(\mathbf{k}) - \hat{P}(\mathbf{k})]^2 \hat{P}(\mathbf{k}) d\mathbf{k} + \mu \int \left[ \frac{[F(\mathbf{k}) - \hat{F}(\mathbf{k})]^2}{[B + \hat{F}(\mathbf{k})]} \right] d\mathbf{k} \quad (63)$$

with an additional factor  $\hat{P}(\mathbf{k})$  in the first integral. It should be stressed that at this time both cost functions (62) and (63) should be regarded only as rather arbitrarily selected candidates which will need to be further tested and possibly modified in more extensive studies.

The solution of the general nonlinear variational problem

$$\frac{\delta J}{\delta F(\mathbf{k})} = 0 \quad (64)$$

was obtained by an iterative technique which made use of the approximate quasi-linear mapping relation (56), as follows.

Starting from a first estimate  $F^1(\mathbf{k}) = \hat{F}(\mathbf{k})$ , let  $F^n(\mathbf{k})$ ,  $P^n(\mathbf{k})$  represent the approximate solution after  $n$  iteration steps, where  $P^n(\mathbf{k})$  is the associated SAR spectrum for the

wave spectrum  $F^n(\mathbf{k})$  in accordance with the fully nonlinear mapping relation (55),

$$P^n = M_{nl}(F^n) \quad (65)$$

Construct now an improved solution

$$F^{n+1} = F^n + \Delta F^n \quad (66)$$

by assuming, in a first step, that the increment  $\Delta F^n$  leads to a modified SAR spectrum

$$P^{n+1} = P^n + \Delta P^n \quad (67)$$

for which the change  $\Delta P^n$  is related to  $\Delta F^n$  through the approximate quasi-linear transformation (equations (56) and (26)),

$$\Delta P^n(\mathbf{k}) = \frac{1}{2} \exp(-k_x^2 \xi_n'^2) [ |T^S(\mathbf{k})|^2 \Delta F^n(\mathbf{k}) + |T^S(-\mathbf{k})|^2 \Delta F^n(-\mathbf{k}) ] \quad (68)$$

Substituting these new estimates for  $F$ ,  $P$  into (62), one obtains

$$J = \int [\Delta P^n - (\hat{P} - P^n)]^2 d\mathbf{k} + \mu \int [\Delta F^n - (\hat{F} - F^n)]^2 d\mathbf{k} \quad (69)$$

The solution of the variational equations for  $J$  with respect to  $\Delta F^n$ , with  $\Delta P^n$  given by (68), can be immediately found:

$$\Delta F^n = \frac{[A_{-\mathbf{k}}(W_{\mathbf{k}} \delta P + \mu \delta F_{\mathbf{k}}) - B_{\mathbf{k}}(W_{-\mathbf{k}} \delta P + \mu \delta F_{-\mathbf{k}})]}{[A_{\mathbf{k}} A_{-\mathbf{k}} - B_{\mathbf{k}}^2]} \quad (70)$$

where

$$\delta P = \hat{P}(\mathbf{k}) - P^n(\mathbf{k}) = \hat{P}(-\mathbf{k}) - P^n(-\mathbf{k}) \quad (71)$$

$$\delta F_{\mathbf{k}} = \hat{F}(\mathbf{k}) - F^n(\mathbf{k}) \quad (72)$$

$$A_{\mathbf{k}} = W_{\mathbf{k}}^2 + 2\mu \quad (73)$$

$$B_{\mathbf{k}} = W_{\mathbf{k}} W_{-\mathbf{k}} \quad (74)$$

and

$$W_{\mathbf{k}} = |T^S(\mathbf{k})|^2 \exp(-k_x^2 \xi_n'^2) \quad (75)$$

Having determined  $\Delta F^n$  and the new wave spectrum  $F^{n+1}$ , the iteration step is then completed by computing the associated SAR spectrum, using the fully nonlinear transformation relation  $P^{n+1} = M_{nl}(F^{n+1})$ .

The technique can be applied equally well to the form (63). In computing the perturbations  $\Delta F^n$ ,  $\Delta P^n$ , the additional factor  $P$  in the first integral in  $J$  is set equal in this case to  $P^n$ .

The iteration scheme was found to converge in all cases studied, including cases with strongly nonlinear and poor first guesses, provided  $\mu$  was not chosen too small, namely,  $\mu \geq \mu_0$ , where

$$\mu_0 = 0.1 \hat{P}_{\max}^2 \quad (76)$$

In most applications, we chose  $\mu = \mu_0$ . The constant  $B$  was set at  $0.01\hat{F}_{\max}$ .

In the Seasat cases discussed in the following section, the SAR calibration was not known. This can be readily accommodated in the inversion formalism by including the dependence on the unknown calibration factor explicitly in the expression for  $J$  and minimizing the cost function simultaneously with respect to both  $F$  and the unknown calibration factor. The minimization with respect to the calibration factor can be given analytically and was carried out after each iteration step.

Other unknown or poorly known parameters  $a_j$  (for example, in the hydrodynamic MTF) can be treated in the same way. If first-guess estimates  $\hat{a}_j$  of these parameters exist, deviations from these values can be penalized by adding standard penalty terms to  $J$  of the form  $\sum_j \mu_j (a_j - \hat{a}_j)^2$ .

The basic inversion formalism can be generalized also in other ways. In practice, it was found that a straightforward application of the inversion method just described yielded wave spectra which successfully reproduced the observed SAR spectra, but were nonetheless clearly unrealistic. The inversion modified the wave spectrum within the wave number region  $|k_x| < k_{x_c}^{\text{cutoff}}$  containing valid SAR information, but left the first-guess wave spectrum unchanged in the high azimuthal wave number region beyond the cutoff. Although entirely consistent with the intended operation of the cost function, the resultant spectra exhibited dislocations along the transitional azimuthal cutoff bands which were obviously spurious.

The origin of these problems is clearly the lack of dynamical constraints in the inversion formalism. In reality, the development of dislocated spectra is prevented by nonlinear wave-wave interactions, which maintain an approximately universal spectral shape in the wind sea region of the spectrum [cf. Hasselmann *et al.*, 1973, 1976; Komen *et al.*, 1984]. The difficulty would not arise if the inversion technique were imbedded in a general wind and wave data assimilation scheme in which all modifications of the wave spectrum were attributed to modifications in the wind field. These would automatically ensure dynamically consistent changes in the wave spectrum through the application of a wave model. This is the ultimate goal of the assimilation program of the Wave Modeling (WAM) Group. However, for the present intermediate level of inversion, without direct coupling to the wind field, some form of dynamical constraints are needed. These were introduced using the following simple two-stage procedure.

As the high wave number region of the spectra is strongly coupled to lower wave numbers through the nonlinear transfer, we restricted the modification of the spectrum in the first inversion stage to transformations which apply uniformly to the entire wave spectrum. The simplest such transformation is a rotation  $\phi_0$  in the wave number plane combined with scale changes  $A$ ,  $B$  in the energy and wave number, respectively.

$$F'(\mathbf{k}) = AF(\mathbf{k}') \quad (77)$$

where

$$\begin{aligned} k'_x &= B(k_x \cos \phi_0 - k_y \sin \phi_0) \\ k'_y &= B(k_x \sin \phi_0 + k_y \cos \phi_0) \end{aligned} \quad (78)$$

After minimizing the cost function with respect to the parameters  $\phi_0$ ,  $A$ ,  $B$ , the original minimization procedure without constraints was then applied in a second stage.

The first stage normally yielded a close fit to the SAR spectral peak, while ensuring continuity of the overall spectral distribution. The second stage then provided further fine-scale adjustments within the azimuthal wave number band for which detailed SAR information was available. Since a reasonable first-order fit was achieved already in the first stage, the second stage no longer produced significant dislocations in the azimuthal cutoff region.

As pointed out earlier, the energy scale parameter  $A$  can be determined rather reliably (for given  $B$ ,  $\phi_0$ ) from the observed azimuthal cutoff scale  $\zeta'$ , which is independent of the details of the SAR spectrum. In practice, the least squares minimization routine was therefore applied in the first stage only to the parameters  $\phi_0$  and  $B$ , while  $A$  was determined explicitly from  $\phi_0$ ,  $B$ , and  $\zeta'$  using the relation (44) for the azimuthal cutoff scale.

## 5. SOME EXAMPLES FROM SEASAT

The computation of the forward transformation relation is illustrated in Figure 3 for a typical Seasat case. The case was selected together with the two other cases discussed in this section from a larger set of SAR image spectra analyzed in the course of a wave hindcast study using the WAM third-generation wave model [WAMDIG, 1988; Hasselmann *et al.*, 1988].

The individual panels show the hindcast WAM wave spectrum, the SAR spectrum computed from the WAM spectrum, and some typical spectral terms of the nonlinear spectral expansion. The case is only weakly nonlinear, so that only little of the azimuthally traveling short wave energy is lost in the SAR image, while most of the wave energy propagating in the range direction is retained. The quasi-linear approximation, consisting of the sum of the first three quasi-linear contributions is seen to yield a fairly good approximation of the fully nonlinear image.

The splitting of the single-wave spectral peak into two peaks in the SAR image spectrum is a common feature in SAR images of predominantly range traveling waves. It arises because the velocity bunching MTF, which normally dominates over the RAR MTF, vanishes in the range direction (cf. section 3 and Figure 2).

The asymmetry of the SAR response about the look direction due to the interference term (cf. Figure 2) is evident in the quasi-linear and fully nonlinear SAR spectra and in the interference term itself. In general, all terms with odd powers of  $(k_x\beta)$  contribute to the asymmetry. As pointed out in section 3, the asymmetry is dependent on the look and flight directions, so that different SAR image spectra are obtained, for example, if the same wave field is viewed from the upwind or downwind direction [Hasselmann *et al.*, 1989]. In comparing Figures 2 and 3, it should be noted that the SAR spectrum is formed from both positive and negative  $\mathbf{k}$  contributions (cf. (26)). Thus in contrast to the filter functions of Figure 2, which apply for only one wave component, the spectra of Figure 3 are symmetrical with respect to the transformation  $\mathbf{k} \rightarrow -\mathbf{k}$ .

The higher order terms in the expansion are proportional to the product of a high power of  $(k_x\beta)$  with the exponential azimuthal cutoff factor and are therefore normally strongly

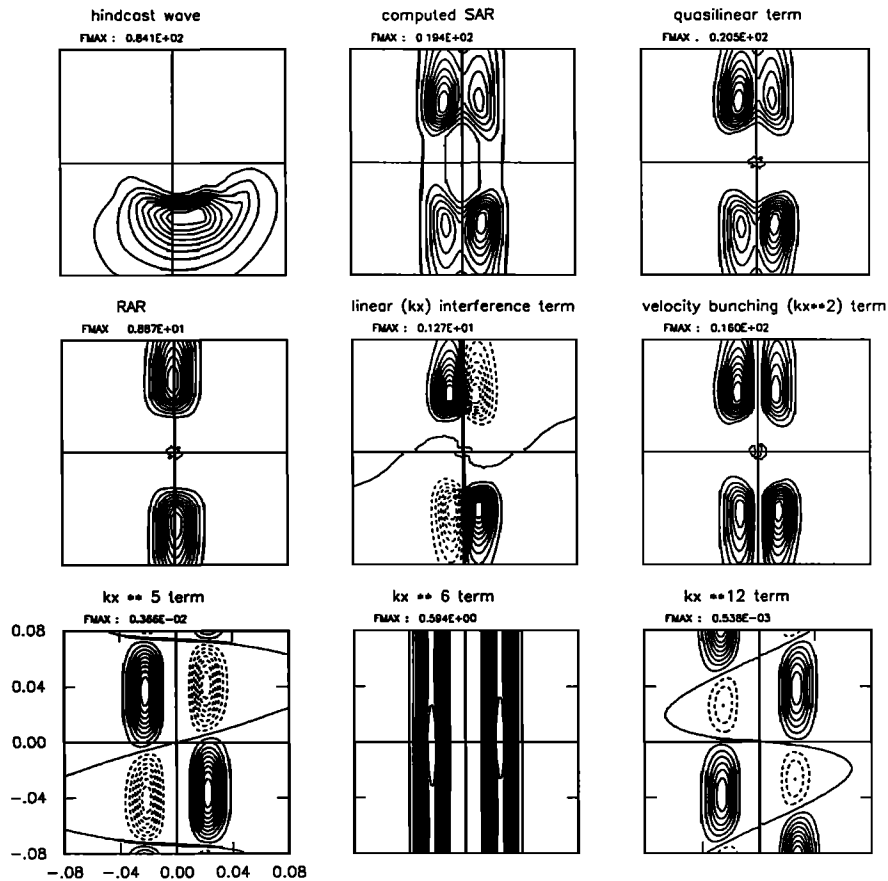


Fig. 3. Hindcast wave spectrum and computed (hindcast) SAR spectra for August 21, 0740, at 57°N, 9°W (top row). Also shown are various spectral expansion terms (see text). The  $x$  axis points in the satellite flight direction, and the  $y$  axis in the negative look direction (right looking SAR).

peaked along the azimuthal cutoff band. These terms do not contribute significantly to the structure of the SAR spectrum in the neighborhood of the spectral peak, so that the effective convergence of the series in the main part of the spectrum is rather rapid (see also Figure 5, discussed below).

Figure 4 shows a comparison of the observed SAR spectra and the computed wave and SAR spectra before and after inversion for the three Seasat cases. Through the combined effects of the azimuthal cutoff, the strongly varying modulation transfer functions (cf. Figure 2) and the nonlinear distortions, the observed and computed SAR spectra (first and third columns, respectively) show relatively little similarity with the hindcast first-guess wave spectra (second column). The first-guess SAR spectra computed from the hindcast wave spectra reproduce the azimuthally banded structure of the observed SAR spectra but nonetheless still show significant deviations.

The fourth and fifth columns show the best fit wave spectra and the associated computed SAR spectra derived by the inversion method. The agreement between the best fit and observed SAR spectra is now seen to be markedly improved. The parameters of the hydrodynamic MTF (6) were chosen in all cases as  $\mu = 0.5 \text{ s}^{-1}$  and  $\gamma = 0$ . This is consistent with field and laboratory measurements [cf. Keller and Wright, 1975; Plant et al., 1983; Feindt et al., 1986; Schröter et al., 1986], but no attempt was made to optimize these parameters. The inversions were based on the peak-enhanced cost function (63).

The three cases were selected to illustrate different degrees of nonlinearity and different directions of wave propagation relative to the SAR look direction. The first case is weakly nonlinear, with predominantly range propagating waves. The second case is moderately nonlinear and represents a wave field propagating at an angle between the range and azimuthal directions. The third case, finally, is strongly nonlinear and was chosen also as an example of a more complex sea state, consisting of a superposition of swell and wind sea components propagating at nearly 90° relative to one another. The azimuthally propagating major swell component is seen to be almost entirely lost due to the azimuthal cutoff.

The individual modifications introduced into the best fit wave spectra through the two-step inversion procedure (summarized in Table 1) can be clearly recognized.

1. The spectra have been rotated and the wave number scales adjusted to reproduce the positions of the SAR spectral peaks.

2. The energy scales have been adjusted (together with the wave number scales) to reproduce the observed azimuthal cutoffs. This effect is evident in the changed azimuthal limits between the first-guess and best fit SAR spectra (columns 3 and 5 of Figure 4).

3. The subsequent modifications of the detailed structures of the spectra, acting separately on all components of the wave spectra, have resulted mainly in some sharpening of the spectral peaks, which were generally too broad in the

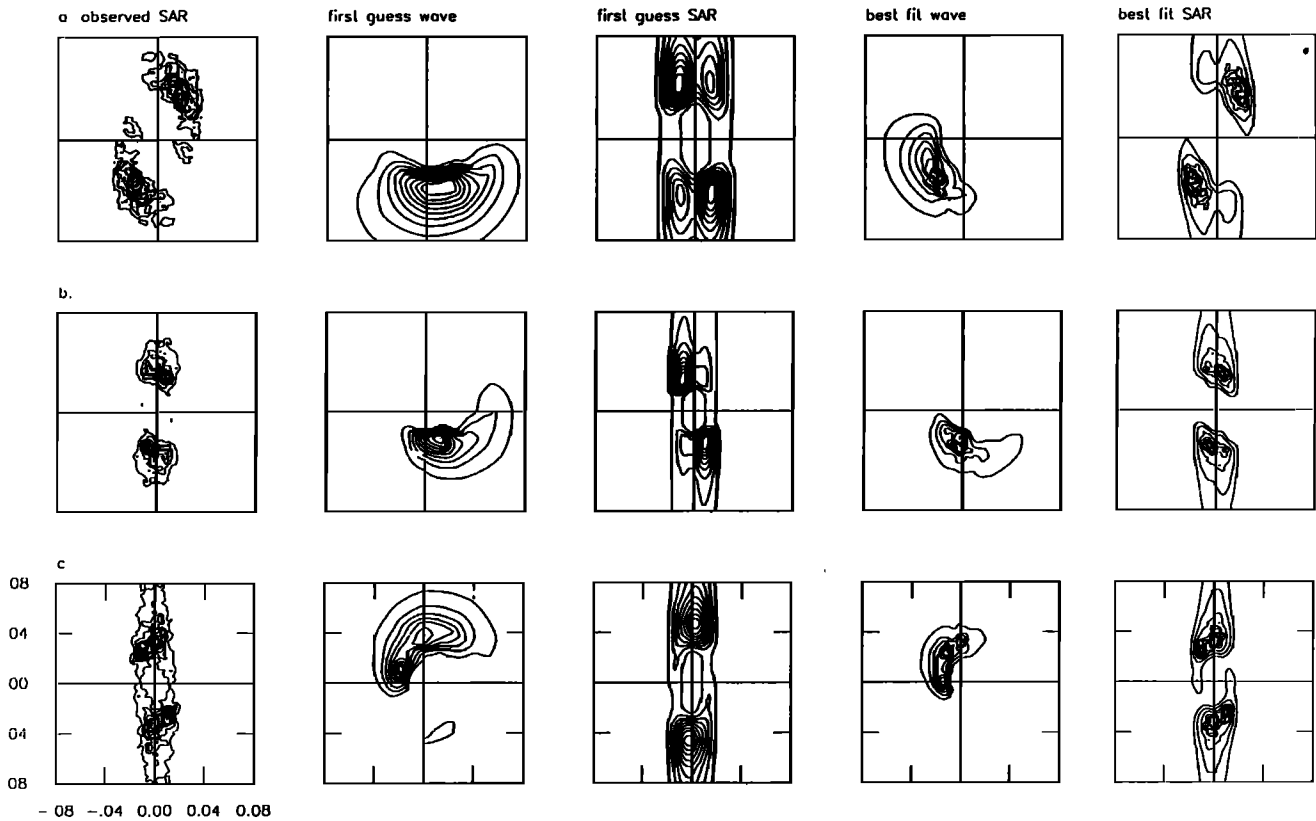


Fig. 4. Observed Seasat SAR spectrum, first-guess (hindcast) wave spectrum, computed first-guess (hindcast) SAR spectrum, and best fit wave and SAR spectra for the case shown in Figure 3 (top row), for August 19, 0620, 60°N, 6°W (second row) and for September 30, 0000, 60°N, 9°W (bottom row).

original wave spectra. (The finite 30° resolution of the WAM model, together with the discrete interaction approximation of the nonlinear transfer source function [cf. *S. Hasselmann et al.*, 1985], are known to result in somewhat too broad peaks in the model spectra.)

The third example illustrates a basic limitation of the present simplified approach, in which a single linear coordinate transformation is applied to the entire spectrum in the first stage of the inversion. The coordinate transformation was governed in this case by the wind sea region of the spectrum, represented by the broad higher frequency peak in the range direction. The peak needed to be rotated about 30° to the left to achieve coincidence between the computed and observed SAR peaks. However, the rotation modified also the azimuthally propagating swell components of the original hindcast wave spectrum, although the swell hindcast was presumably not directly affected by errors in the wind sea hindcast. This deficiency could in principle have been overcome by considering a more sophisticated class of transformations. However, this was not pursued further, since, as has been pointed out, it is anticipated that the present

two-stage inversion procedure will be ultimately superseded by a comprehensive data assimilation scheme in which the measured SAR spectrum is used to modify the wind field rather than the wave spectrum directly.

The convergence properties of the spectral expansion (50) for the three cases considered are indicated in Figure 5. Terms of different nonlinearity order  $n$  for a given velocity bunching order  $m$  (which appear in the same Fourier transform contribution) have been collected into a single term. The curves show the maximal spectral values for each  $m$ th-order spectrum of the expansion. Since these values, as already mentioned, tend to lie near the relatively unimportant azimuthal cutoff limits for the higher order expansion terms, the effective convergence is in fact better than implied by the figure. In practice, good convergence was achieved in all cases studied with a truncation of the series at  $m = 12(n = 6, 7)$ .

6. CONCLUSIONS

The new closed, nonlinear integral transformation relation derived in this paper, together with its expansion in a

TABLE 1. Inversion Parameters of Seasat SAR Spectra

Case	Seasat Swath	Latitude, deg N	Longitude, deg W	Date	Time, UT	$\phi_0$ , deg	$B$	$A$
<i>a</i>	794	57	9	Aug. 21	0740	64	1.2	0.75
<i>b</i>	762	60	6	Aug. 19	0620	33	1.1	1.6
<i>c</i>	1359	60	9	Sept. 30	0000	-28	1.5	1.3

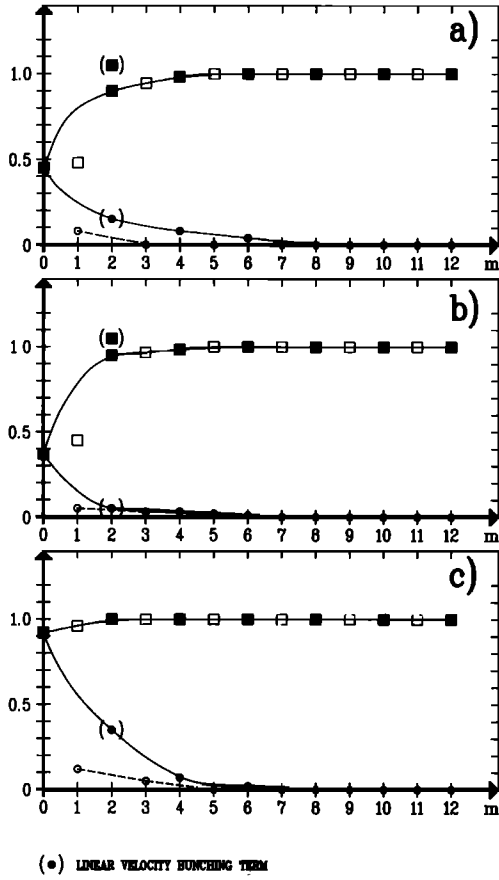


Fig. 5. Convergence of the spectral series expansions with respect to velocity bunching order  $m$ . Plotted are the maximal values of each spectrum. Squares denote the partial sum, dots the contribution of the last term in the sum. Solid and open points refer to even and odd  $m$ , respectively. The convergence in the neighborhood of the spectral peak of the net SAR spectrum is faster than indicated by the individual maximal values.

spectral series with respect to nonlinearity and velocity bunching order, presents a number of advantages.

1. It can be computed rather rapidly using fast Fourier transforms and is free of the statistical sampling errors of Monte Carlo methods. It should thus make feasible the operational processing of SAR wave images which will be obtained from future satellites such as ERS-1, 2, and Radar-sat.

2. It provides a clearer insight into the imaging mechanism by identifying the different contributions from the RAR modulation and nonlinear velocity bunching processes and their various interference terms.

3. It yields a simple expression for the azimuthal cutoff in the form of a Gaussian filter factor which acts on all terms in the series expansion. The azimuthal cutoff scale is given by the rms azimuthal velocity bunching displacement. The observed azimuthal cutoff therefore yields a useful integral constraint on the wave spectrum.

4. The lowest order quasi-linear term of the spectral series expansion, consisting of the product of the standard linear SAR spectrum and the azimuthal cutoff factor, yields a useful first-order approximation of the fully nonlinear mapping relation.

5. It provides the necessary basis for inverting the transformation using standard inverse modeling techniques.

Because of the  $180^\circ$  ambiguity of the spectral mapping relation and the loss of information beyond the azimuthal cutoff, an inversion of the wave-to-image transformation will in general be feasible only if a first-guess wave spectrum is available. This implies that the interpretation and application of SAR wave image data will normally require the application of a wave model.

The inversion technique developed in this study provides an optimal wave spectral estimate for a given first-guess wave spectrum and observed SAR spectrum. The examples shown demonstrate that SAR ocean wave images can indeed provide valuable information to correct modeled wave spectra.

No attempt was made at this stage to correct for possible deficiencies in the wind field driving the wave model, which will normally be the principal cause of discrepancies between observed and predicted SAR spectra. The present inversion technique requires additional ad hoc assumptions to replace the dynamical constraints which would be introduced automatically if the inversion method were integrated in a general wind and wave data assimilation scheme. The inversion technique presented here should therefore be regarded only as an intermediate step toward the development of such a comprehensive data assimilation system.

#### APPENDIX: EXTENSION TO ACCELERATION SMEARING AND GENERAL DISPERSIVE MAPPING

The pure velocity bunching theory presented in section 3 is nondispersive: an infinitesimal cross-section element  $\sigma(\mathbf{r}') d\mathbf{r}'$ , which in the absence of motion effects would correspond to an image element  $\hat{I}^R(\mathbf{r}') d\mathbf{r}' = \sigma(\mathbf{r}') d\mathbf{r}'/\bar{\sigma}$ , is mapped one-to-one into a displaced infinitesimal element

$$\hat{I}^S(\mathbf{r}) d\mathbf{r} = \hat{I}^R(\mathbf{r}') d\mathbf{r}' \quad (\text{A1})$$

in the SAR image plane, where

$$\mathbf{r} = \mathbf{r}' + \boldsymbol{\xi}(\mathbf{r}') \quad (\text{A2})$$

and  $\boldsymbol{\xi} = \mathbf{a}\beta v$  (equation (14)).

In the general SAR theory of ocean wave imaging for arbitrarily moving scattering elements, the mapping is dispersive (cf. MSR): an infinitesimal element on the sea surface is mapped into a finite patch in the SAR image plane. The form (A1) must accordingly be generalized to the integral relation

$$\hat{I}^S(\mathbf{r}) = \int \hat{I}^R(\mathbf{r}') M(\mathbf{r} - \mathbf{r}'; \mathbf{r}') d\mathbf{r}' \quad (\text{A3})$$

The mapping function  $M(\mathbf{r} - \mathbf{r}'; \mathbf{r}')$  represents a finite width distribution with respect to the primary spatial separation variable  $\mathbf{r} - \mathbf{r}'$  and depends in general also on the details of the motion history of the scattering element at  $\mathbf{r}'$ . To a good approximation, the shape of  $M$  is given by the shape of the Doppler spectrum of the backscattered return signal (MSR).

In the nondispersive velocity bunching model, the Doppler spectrum is a line spectrum, and  $M$  therefore reduces to a  $\delta$  function,

$$M(\mathbf{r} - \mathbf{r}'; \mathbf{r}') = \delta[\mathbf{r} - \mathbf{r}' - \boldsymbol{\xi}(\mathbf{r}')] \quad (\text{A4})$$

In the general case, the time dependence of the backscattering elements cannot be represented simply as the constant advection of a frozen scatterer, and the Doppler spectrum and mapping function  $M$  have finite width.

For Bragg scattering, the assumption of a constant advection velocity given by the instantaneous orbital velocity in the center of the viewing window nevertheless remains a good first approximation. The pure velocity bunching theory is therefore normally generalized by expanding the change in orbital velocity during the SAR viewing interval  $-\tau/2 < t < \tau/2$  in a Taylor series,

$$v(\mathbf{r}, t) = v(\mathbf{r}, 0) + ta(\mathbf{r}, 0) + \dots \quad (\text{A5})$$

where  $a(\mathbf{r}, 0) = [dv(\mathbf{r}, t)/dt]_{t=0}$  represents the orbital acceleration (in the range direction) in the center of the viewing window. It is assumed that  $\tau$  is small compared with the wave period.

The linear drift of the orbital velocity during the SAR illumination time leads to an approximately uniform azimuthal smearing of the scattering element in the image plane over the interval  $\xi - \beta|a|\tau/2 < x < \xi + \beta|a|\tau/2$ . The mapping function in this case becomes

$$M^h(\mathbf{r} - \mathbf{r}'; \mathbf{r}') = \delta(y - y') H\left(\frac{x - x' - \xi(\mathbf{r}')}{\beta|a|\tau}\right) (\beta|a|\tau)^{-1} \quad (\text{A6})$$

where  $H(\eta)$  denotes the top hat function

$$H(\eta) = 1 \quad |\eta| \leq \frac{1}{2} \quad (\text{A7})$$

$$H(\eta) = 0 \quad |\eta| > \frac{1}{2}$$

In place of (A6), a Gaussian distribution

$$M^g(\mathbf{r} - \mathbf{r}'; \mathbf{r}') = (2\pi)^{-1/2} (\Delta x)^{-1} \exp\left\{-\frac{[x - x' - \xi(\mathbf{r}')]^2}{2(\Delta x)^2}\right\} \delta(y - y') \quad (\text{A8})$$

with the same rms width

$$\Delta x(\mathbf{r}') = \frac{\beta\tau|a(\mathbf{r}')|}{2(3)^{1/2}} \quad (\text{A9})$$

as the top hat form (A6) is sometimes used [cf. *Alpers and Brüning*, 1986]. This simplifies the treatment of acceleration smearing within the framework of a more general analysis, including the effects of the antenna pattern and the matched filter and other SAR system characteristics.

The distinction between (A6) and (A8) is immaterial in the present context. We shall show that if the function  $M$  is known, regardless of the model used, the surface wave-SAR image spectral mapping relations can be derived as before in closed form.

Starting from the general form (A3), the expression (28) for the Fourier components of the SAR image now becomes (for  $\mathbf{k} \neq 0$ , so that  $I(\mathbf{r})$  may be replaced by  $\hat{I}(\mathbf{r})$ )

$$I_{\mathbf{k}}^S = \frac{1}{A} \int d\mathbf{r} \hat{I}^S(\mathbf{r}) \exp(-i\mathbf{k} \cdot \mathbf{r}) = \frac{1}{A} \iint d\mathbf{r} d\mathbf{r}' \hat{I}^R(\mathbf{r}') M(\mathbf{r} - \mathbf{r}'; \mathbf{r}') \exp(-i\mathbf{k} \cdot \mathbf{r}) \quad (\text{A10})$$

or

$$I_{\mathbf{k}}^S = \frac{1}{A} \int d\mathbf{r}' \hat{I}^R(\mathbf{r}') G_{\mathbf{k}}(\mathbf{r}') \exp(-i\mathbf{k} \cdot \mathbf{r}') \quad (\text{A11})$$

where

$$G_{\mathbf{k}}(\mathbf{r}') = \int d\rho M(\rho; \mathbf{r}') \exp(-i\mathbf{k} \cdot \rho) \quad (\text{A12})$$

The nonlinearity of the imaging relation (A11) arises through the dependence of the weighting function  $G_{\mathbf{k}}(\mathbf{r}')$  on the local wave field at  $\mathbf{r}'$ .

For the two forms (A6) for  $M^h$  or (A8) for  $M^g$ , we obtain the weighting functions

$$G_{\mathbf{k}}^h(\mathbf{r}') = \exp[-i\mathbf{k} \cdot \xi(\mathbf{r}')] \frac{\sin[(3)^{1/2} k_x |\Delta x|]}{(3)^{1/2} k_x |\Delta x|} \quad (\text{A13})$$

$$G_{\mathbf{k}}^g(\mathbf{r}') = \exp[-i\mathbf{k} \cdot \xi(\mathbf{r}')] \exp\left(\frac{-k_x^2 \Delta x^2}{2}\right) \quad (\text{A14})$$

Thus the velocity bunching mapping factor  $\exp[-i\mathbf{k} \cdot \xi(\mathbf{r}')] in (28) is replaced now in the general case by a mapping factor$

$$G_{\mathbf{k}}^{h,g} = \exp[-i\mathbf{k} \cdot \xi(\mathbf{r}')] D^{h,g} \quad (\text{A15})$$

which contains an additional azimuthal acceleration smearing term

$$D^h = \frac{\sin[(3)^{1/2} k_x |\Delta x|]}{(3)^{1/2} k_x |\Delta x|} \quad (\text{A16})$$

or

$$D^g = \exp\left(\frac{-k_x^2 \Delta x^2}{2}\right) \quad (\text{A17})$$

The further analysis proceeds as in section 3, with the velocity bunching weighting function  $\exp[-i\mathbf{k} \cdot \xi(\mathbf{r}')] replaced by the general weighting function  $G_{\mathbf{k}}$ . The expression (30) for the SAR image variance spectrum becomes$

$$P_{\mathbf{k}}^S = A^{-2} \left\{ \iint d\mathbf{r}' d\mathbf{r}'' \exp[-i\mathbf{k}(\mathbf{r}' - \mathbf{r}'')] \cdot N_{\mathbf{k}} D(\mathbf{r}') D(\mathbf{r}'') \left\{ 1 + \sum_{\mathbf{k}'} (T_{\mathbf{k}'}^R \zeta_{\mathbf{k}'} + T_{-\mathbf{k}'}^{R*} \zeta_{-\mathbf{k}'}^*) e^{i\mathbf{k}' \cdot \mathbf{r}'} \right\} \cdot \left\{ 1 + \sum_{\mathbf{k}''} (T_{\mathbf{k}''}^{R*} \zeta_{\mathbf{k}''}^* + T_{-\mathbf{k}''}^R \zeta_{-\mathbf{k}''}) e^{-i\mathbf{k}'' \cdot \mathbf{r}''} \right\} \right\} \quad (\text{A18})$$

The expression differs from (30) only through the inclusion of the acceleration smearing factors  $D(\mathbf{r}') D(\mathbf{r}'')$ .

To evaluate the expectation value occurring on the right-hand side of (A18), the same technique may be applied as before. The product  $D(\mathbf{r}')D(\mathbf{r}'')$  is first expanded in a power series with respect to the wave Fourier amplitudes. For the forms (A16) or (A17), this is straightforward. The expectation value of the product of  $N_{\mathbf{k}}$  with the various wave amplitude products occurring in the rest of the integrand in (A18) is then again computed by expanding  $N_{\mathbf{k}}$  with respect to the particular infinitesimal wave amplitude components appearing in any given product.

The only difference between the extended theory and the previous pure velocity bunching theory is that the wave amplitude products with which  $N_{\mathbf{k}}$  is now correlated are no longer limited to linear and quadratic expressions, as in (32)–(34), but consist of an infinite series. Since it was already found convenient, both theoretically and computationally, to expand the closed integral expression (46) for the pure velocity bunching case in a spectral power series, the present extension involves no significant algebraic or computational overhead. The expansion algebra can be readily incorporated in the (computer coded) algebra used to generate the expansion (50) with respect to velocity bunching and nonlinearity order. The structure of the expansion remains basically unchanged except for the appearance of a third expansion parameter, the ratio of the SAR illumination time  $\tau$  to the mean wave period.

*Acknowledgments.* We are grateful for several suggested clarifications to the first version of this paper by the reviewers and for useful discussions with Claus Brüning. This work was partly supported by the U.S. Office of Naval Research through grant N00014-88-J-1025.

#### REFERENCES

- Alpers, W., Monte Carlo simulations for studying the relationship between ocean wave and synthetic aperture radar image spectra, *J. Geophys. Res.*, **88**, 1745–1759, 1983.
- Alpers, W., and C. Brüning, On the relative importance of motion-related contributions to the SAR imaging mechanism of ocean surface waves, *IEEE Trans. Geosci. Remote Sensing*, **GE-24**, 873, 1986.
- Alpers, W., and K. Hasselmann, Spectral signal-to-clutter and thermal noise properties of ocean wave imaging synthetic aperture radars, *Int. J. Remote Sensing*, **3**, 423–446, 1982.
- Alpers, W., and C. L. Rufenach, The effect of orbital motions on synthetic aperture radar imagery of ocean waves, *IEEE Trans. Antennas Propag.*, **AP-27**, 685–690, 1979.
- Alpers, W., D. B. Ross, and C. L. Rufenach, On the detectability of ocean surface waves by real and synthetic aperture radar, *J. Geophys. Res.*, **86**, 6481–6498, 1981.
- Alpers, W., C. Brüning, and K. Richter, Comparison of simulated and measured synthetic aperture radar image spectra with buoy-derived ocean wave spectra during the Shuttle Imaging Radar-B mission, *IEEE Trans. Geosci. Remote Sensing, SIR-B Spec. Issue*, **GE-24**, 559, 1986.
- Beal, R. C., D. G. Tilley, and F. M. Monaldo, Large- and small-scale spatial evolution of digitally processed ocean wave spectra from Seasat Synthetic Aperture Radar, *J. Geophys. Res.*, **88**, 1761–1778, 1983.
- Brüning, C., W. Alpers, L. F. Zambresky, and D. G. Tilley, Validation of a synthetic aperture radar ocean wave imaging theory by the Shuttle Imaging Radar-B experiment over the North Sea, *J. Geophys. Res.*, **93**, 15,403–15,425, 1988.
- Brüning, K., W. Alpers, and K. Hasselmann, Monte Carlo simulation studies of the nonlinear imaging of a two-dimensional surface wave field by a synthetic aperture radar, *Int. J. Remote Sensing*, **11**, 1695–1727, 1990.
- Donelan, M. A., J. Hamilton, and W. H. Hui, Directional spectra of wind-generated waves, *Philos. Trans. R. Soc. London, Ser. A*, **315**, 509–562, 1985.
- Feindt, F., Radar-Rückstreuexperimente am Wind-Wellen-Kanal bei sauberer und filmbedeckter Wasseroberfläche im X-Band (9.8 GHz), Ph.D. thesis, Hamburg Univ., Germany, 1985.
- Feindt, F., J. Schröter, and W. Alpers, Measurement of the ocean wave-radar modulation transfer function at 35 GHz from a sea-based platform in the North Sea, *J. Geophys. Res.*, **91**, 9701–9708, 1983.
- Hasselmann, K., et al., Measurements of wind-wave growth and swell decay during the Joint North Sea Wave Project (JONSWAP), *Ergänzungsh. Dtsch. Hydrogr. Z., Reihe A(8)*, no. 12, 1973.
- Hasselmann, K., D. B. Ross, P. Müller, and W. Sell, A parametric wave prediction model, *J. Phys. Oceanogr.*, **6**, 200–228, 1976.
- Hasselmann, K., R. K. Raney, W. J. Plant, W. Alpers, R. A. Shuchman, D. R. Lyzenga, C. L. Rufenach, and M. J. Tucker, Theory of synthetic aperture radar ocean imaging: A MARSEN view, *J. Geophys. Res.*, **90**, 4659–4686, 1985.
- Hasselmann, K., S. Hasselmann, E. Bauer, C. Brüning, S. Lehner, H. Graber, and P. Lionello, Development of a satellite SAR image spectra and altimeter wave height data assimilation system for ERS-1, *MPI Rep. 19*, Max-Planck-Inst. für Meteorol., Hamburg, Germany, 1988.
- Hasselmann, K., S. Hasselmann, C. Brüning, and A. Speidel, Application of a new closed ocean wave-SAR spectral transform relation to LEWEX data, paper presented at Conference on measuring, modeling, predicting and applying directional ocean wave spectra, Johns Hopkins Univ., Baltimore, Md., April 18–20, 1989.
- Hasselmann, K., S. Hasselmann, and K. Barthel, Use of a wave model as a validation tool for ERS-1 AMI wave products and as input for the ERS-1 wind retrieval algorithms, *MPI Rep. 55*, 96 pp., Max-Planck-Inst. für Meteorol., Hamburg, Germany, 1990.
- Hasselmann, S., K. Hasselmann, J. H. Allender, and T. P. Barnett, Computations and parameterizations of the nonlinear energy transfer in a gravity wave spectrum, II. Parameterizations of the nonlinear energy transfer for application in wave models, *J. Phys. Oceanogr.*, **15**, 1378–1391, 1985.
- Holthuijsen, L. H., Observations of the directional distribution of ocean-wave energy in fetch-limited conditions, *J. Phys. Oceanogr.*, **13**, 191–207, 1983.
- Jackson, F. C., An analysis of short pulse and dual frequency radar techniques for measuring ocean wave spectra from satellites, *Radio Sci.*, **16**, 1385–1400, 1981.
- Jackson, F. C., W. T. Walton, and P. L. Baker, Aircraft and satellite measurement of ocean wave directional spectra using scanning-beam microwave radars, *J. Geophys. Res.*, **90**, 987–1004, 1985a.
- Jackson, F. C., W. T. Walton, and C. Y. Peng, A comparison of in situ and air-borne radar observations of ocean wave directionality, *J. Geophys. Res.*, **90**, 1005–1018, 1985b.
- Keller, W. C., and J. W. Wright, Microwave scattering and the straining of wind-generated waves, *Radio Sci.*, **10**, 139–147, 1975.
- Kenney, J. E., E. A. Uliana, and E. J. Walsh, The surface contour radar: A unique remote sensing instrument, *IEEE Trans. Microwave Theory Techniques*, **MTT 27**, 1080–1092, 1979.
- Komen, G. J., S. Hasselmann, and K. Hasselmann, On the existence of a fully developed wind-sea spectrum, *J. Phys. Oceanogr.*, **14**, 1271–1285, 1984.
- Lamb, H., *Hydrodynamics*, 6th ed., 738 pp., Dover, New York, 1932.
- Lyzenga, D. R., Numerical simulation of synthetic aperture radar image spectra for ocean waves, *IEEE Trans. Geosci. Remote Sensing*, **GE-24(6)**, 863–871, 1986.
- Monaldo, F. M., and D. R. Lyzenga, On the estimation of slope- and height-variance spectra from SAR imagery, *IEEE Trans. Geosci. Remote Sensing*, **GE-24**, 543–551, 1986.
- Monaldo, F. M., and D. R. Lyzenga, Comparison of shuttle imaging radar-B ocean wave spectra with linear model predictions based on aircraft measurements, *J. Geophys. Res.*, **93**, 374–388, 1988.
- Pierson, W. J., Jr., and L. Moskowitz, A proposed spectral form for fully developed wind seas based on the similarity theory of S. A. Kitaigorodskii, *J. Geophys. Res.*, **69**, 5181–5190, 1964.
- Plant, W. J., The microwave measurement of ocean-wave directional spectra, *Johns Hopkins APL Tech. Dig.*, **8(1)**, 55–59, 1987.
- Plant, W. J., W. C. Keller, and A. Cross, Parametric dependence of

- the ocean wave radar modulation transfer function, *J. Geophys. Res.*, *88*, 9747–9756, 1983.
- Raney, R. K., Wave orbital velocity, fade, and SAR response to azimuth waves, *IEEE J. Oceanic Eng.*, *OE-6*, 140–146, 1981.
- Rosenthal, W., F. Ziemer, K. Raney, and P. Vachon, Removal of 180° ambiguity in SAR images of ocean waves, paper presented at IGARSS '89, Remote Sensing: An Economic Tool for the Nineties, Vancouver, Canada, July 10–14, 1989.
- Schröter, J., F. Feindt, W. Alpers, and W. C. Keller, Measurement of the ocean wave–radar modulation transfer function at 4.3 GHz, *J. Geophys. Res.*, *91*, 932–946, 1986.
- Swift, C. F., and L. R. Wilson, Synthetic aperture radar imaging of moving ocean waves, *IEEE Trans. Antennas Propag.*, *AP-27*, 725–729, 1979.
- Tucker, M. J., The imaging of waves by satellite synthetic aperture radar: The effects of surface motion, *Int. J. Remote Sensing*, *6*, 1059–1074, 1985.
- Vachon, P. W., and R. K. Raney, Resolution of ocean wave propagation direction in single-pass airborne SAR imagery, paper presented at IGARSS '89, Remote Sensing: An Economic Tool for the Nineties, Vancouver, Canada, July 10–14, 1989.
- Valenzuela, G. R., An asymptotic formulation for SAR images of the dynamical ocean surface, *Radio Sci.*, *15*, 105–114, 1980.
- Walsh, E. J., D. W. Hancock III, D. E. Hines, R. N. Swift, and J. F. Scott, Directional wave spectral measured with the surface contour radar, *J. Phys. Oceanogr.*, *15*, 566–592, 1985.
- Walsh, E. J., D. W. Hancock III, D. E. Hines, R. N. Swift, and J. F. Scott, Wave-measurement capabilities of the surface contour radar and the air-borne oceanographic Lidar, *Johns Hopkins APL Tech. Dig.*, *8*(1), 74–81, 1987.
- Walsh, E. J., D. W. Hancock III, D. E. Hines, R. N. Swift, and J. F. Scott, Evolution of the directional wave spectrum from shoreline to fully developed, *J. Phys. Oceanogr.*, in press, 1991.
- WAMDIG, The WAM model—A third generation ocean wave prediction model, *J. Phys. Oceanogr.*, *18*, 1775–1810, 1988.
- Wright, J. W., A new model for sea clutter, 1968, *IEEE Trans. Antennas Propag.*, *AP-16*, 217–223, 1968.
- 
- K. Hasselmann and S. Hasselmann, Max-Planck-Institut für Meteorologie, Bundesstrasse 55, W-2000 Hamburg 13, Germany.

(Received August 14, 1990;  
revised January 28, 1991;  
accepted January 28, 1991.)